electronics

Article

ASILO-Based Active Fault-Tolerant Control of Spacecraft Attitude with Resilient Prescribed Performance

Ze Yang [1,*], Baoqing Yang [1], Ruihang Ji [2] and Jie Ma [1,*]

[1] School of Astronautics, Harbin Insitute of Technology, 92 Xidazhi Street, Harbin 150001, China; ybq@hit.edu.cn
[2] Department of Electrical and Computer Engineering, National University of Singapore, 21 Lower Kent Ridge Rd, Singapore 117576, Singapore; jiruihang@nus.edu.sg
* Correspondence: 20b904028@stu.hit.edu.cn (Z.Y.); majie@hit.edu.cn (J.M.)

Abstract: In this study, an active fault-tolerant control problem was addressed for a rigid spacecraft in the presence of unknown actuator faults, uncertainties, and disturbances. First, an adaptive sliding mode iterative learning-based observer (ASILO) is proposed for diagnosing and reconstructing unknown faults. It achieves greater accuracy and rapidity while consuming less computing resources by constructing adaptive gain based on an auxiliary error. Specifically, it significantly improved the computational efficiency by 76% compared with the Strong Tracking Kalman Filter while achieving a similar accuracy. It also enhanced the accuracies relative to the traditional ILO and adaptive ILO by 67% and 36%, respectively, and demonstrated 82% and 52% increases in rapidity. Then, fault-tolerant control with resilient prescribed performance (RPP) that can adapt to changing initial conditions and adaptively adjust performance constraints online by sensing faults and error trends is proposed. It avoided the control singularity by constructing adaptive resilient boundaries with almost no impact on the computational overhead. It significantly improved the performance and conservatism. Finally, the robustness and effectiveness of the proposed strategy were demonstrated by numerical simulations.

Keywords: spacecraft; attitude control; fault reconstruction; iterative learning; prescribed performance; fault tolerant control

check for updates

Received: 11 December 2024
Revised: 29 December 2024
Accepted: 2 January 2025
Published: 4 January 2025

Citation: Yang, Z.; Yang, B.; Ji, R.; Ma, J. ASILO-Based Active Fault-Tolerant Control of Spacecraft Attitude with Resilient Prescribed Performance. *Electronics* **2025**, *14*, 181. https://doi.org/10.3390/electronics14010181

1. Introduction

With the expansion of space tasks, such as asteroid exploration, Earth environment monitoring, and managing satellite internet constellations, the demand for the high performance of spacecraft continues to increase [1]. The attitude control system (ACS) has been extensively researched and studied regarding how to maintain stable operation and maximize its remaining performance when faults occur [2]. Currently, widely used fault-handling methods mainly rely on ground-tracking stations to diagnose faults by analyzing telemetry data, and then reconfigure the spacecraft [3], which is essentially human-in-the-loop fault-tolerant control. This approach is time-consuming and performs poorly, making it unsuitable for future scenarios involving numerous on-orbit spacecraft and high communication delays. The pursuit of high reliability has led to many methods proposed to achieve fault-tolerant control (FTC), which can usually be classified into passive fault-tolerant control (PFTC) and active fault-tolerant control (AFTC) [4,5]. PFTC makes the system as insensitive as possible to potential known faults by designing a fixed controller, which has low complexity and is easy to implement [6]. Due to its reliance on pre-designed fault scenarios and redundancy mechanisms, PFTC is effective only for known, fixed, and predictable faults [7]. However, the space environment in which spacecraft operate is typically dynamic and unpredictable. Unforeseen time-varying disturbances and faults, such as those caused by cosmic rays, gravity, and micrometeoroids [1,2], are in direct contrast to the static environment that PFTC is designed to handle. In the dynamic and unpredictable space environment, PFTC introduces excessive redundancy and constraints to ensure robustness and stability, which slows down the response and affects the trajectory-tracking accuracy and mission efficiency. Furthermore, in the absence of faults, this redundancy hinders system performance by underutilizing hardware capabilities. Additionally, the static nature of PFTC reduces its adaptability, hindering timely adjustments to rapidly changing external conditions and further degrading the overall system performance. All these ultimately lead to its strong conservatism, which limits its performance. By contrast, AFTC needs to design the fault diagnosis, isolation, and reconstruction (or estimation) (FDIR) module and reconfigure the controller according to the real-time diagnosis results, which can achieve optimal performance and higher flexibility, and thus, is more suitable for spacecraft [8]. However, the accuracy and speed of FDIR directly affect the control performance, and more efficient fault reconstruction of a nonlinear system remains a challenge.

Model-driven FDIR was proposed by Beard [9,10] in the 1970s, which can take advantage of analytical redundancy rather than complex and expensive hardware redundancy. Given the pre-established mathematical model during the design phase, model-driven FDIR has attracted significant attention and research, such as the robust residual generator in [11] applied to the Mars Express spacecraft to detect faults. The adaptive observer (AO) proposed in [12] and the sliding mode observer (SMO) in [13] can estimate sensor faults relatively accurately, but is still limited to linear systems. The extended Kalman filter (EKF) [14], unscented Kalman filter (UKF) [15], and cubature Kalman filter (CKF) [16] are also used for more accurate actuator fault reconstruction. Furthermore, the improved CKF can achieve fast and accurate FDIR under complex disturbances [17], but the cost is a greater computational cost. A linear ILO [18] and nonlinear time-invariant ILO [19–21] were respectively designed to diagnose actuator faults. The use of constant gains leads to issues such as slow convergence, chattering, and reduced accuracy. An adaptive ILO (AILO) was designed in [22,23], but when applied to FDIR, the performance can still be further improved. The AO structure is complex and difficult to design, while the SMO, though robust, still could not meet the convergence speed requirements for FDIR in this study. EKF, due to linearization, is unsuitable for highly nonlinear systems. On the other hand, the UKF, CKF, and STCKF introduce excessive computational complexity due to sampling, integration, and matrix decomposition, making it incompatible with onboard hardware. In contrast, the ILO offers simpler design and greater flexibility, making it easier to balance complexity and performance. Therefore, this study drew upon AO and SMO concepts, focusing on introducing adaptive gains and constructing auxiliary errors to improve the ASILO approach.

In terms of FTC, compared with methods such as adaptive control [24,25], sliding mode control (SMC) [26–28] has the advantages of rapid response, robustness to uncertainty, and a simple design. However, it is still impossible to directly constrain the desired transient and steady-state performance during the design. Prescribed performance control (PPC) [29] and funnel control [30] enable the controller to meet the desired performance, such as accuracy and overshoot. Meanwhile, PPC can be combined with other control methods to complement each other [31–33]. PPC was applied to AFTC and good results were achieved [34–36]. However, PPC has many shortcomings [37,38], such as the inability to achieve finite time convergence and control singularities caused by faults. When the error inevitably breaks through the static boundary due to faults or disturbances and causes instability, it is called a control singularity, which is a unique issue of PPC that needs to be solved. Refs. [39–41] propose appointed-time PPC to enable a controller to converge to the performance constraint range within a finite time. An auxiliary system was implemented [42] to adjust the boundary to accommodate the possible increase in error, but it did not fully exploit the error trend information and did not consider adaptation to arbitrary initial states and convergence in the appointed time. Ref. [43] improves PPC so that it can adaptively adjust the boundary to avoid control singularities, but its boundary corrections generated using only errors may occasionally result in untimely adjustments or premature narrowing, resulting in insufficient applicability. Ref. [30] achieved excellent adaptive adjustment of the funnel boundary with low complexity to handle saturation in the scheme of funnel control. However, funnel control seems to be lacking in the characterization of complex performance constraints. This paper expands it to the PPC and uses asymmetric boundaries to constrain the overshoot and convergence time. Ref. [44] proposes an approximation-free adaptive PPC to cope with saturation and achieved good results, but it is not convenient for appointed-time performance constraints due to the differential equations design. Also, entry capture [32] is not adequately considered to accommodate variable initial errors in the above results. However, the above results cannot achieve multiple goals at the same time.

An analysis found that the control singularity is caused by fault-induced actuator saturation, which is not a significant issue for other control methods but renders PPC ineffective. Unlike approaches focused on mitigating input saturation, such as introducing auxiliary systems [25,45] or using backstepping [46] to design virtual commands, this paper emphasizes how to leverage the automatic adjustment of PPC boundaries during saturation to prevent errors from exceeding these boundaries, thereby maintaining stability. Building on these ideas, we propose an improved AFTC scheme that includes an improved adaptive sliding mode iterative observer (ASILO) and fault-tolerant control based on resilient prescribed performance (RPP). The key contributions of this paper are as follows:

- The proposed ASILO for reconstructing actuator faults includes the design of fast auxiliary error and adaptive gain. Compared with existing methods [19–23], it enhances the reconstruction accuracy and speed without a substantial increase in the computational demand, which is relatively more friendly to spacecraft engineering.
- The proposed RPP enables user-driven adjustments of transient and steady performances. Its resilient correction capability autonomously adjusts the performance boundaries in response to detected faults and error changes rather than designing anti-saturation control. The initialization mechanism adaptively sets initial boundaries before control, obviating manual intervention. Compared with [37–39], this approach effectively resolves the control singularity and initial capture issues inherent in static PPC.
- Fault-tolerant control with RPP is developed, whose performance including the convergence time, overshoot, and steady-state error is guaranteed and designed. The control singularity problem under initial constraint violation and actuator faults is addressed. This improves the conservatism and robustness.

This paper is organized as follows. Section 2 provides the problem description and preliminaries. The main results of this work are presented in Section 3, including the design of the ASILO and FTC with RPP. Section 4 presents the comparative numerical simulation results, demonstrating the effectiveness of the proposed method. Finally, Section 5 summarizes the conclusions and future investigation.

2. Problem Statement and Preliminaries

Consider a class of ACS of a spacecraft with uncertainty, disturbance, and actuator faults. The actuators are reaction wheels or control moment gyros. In addition, the inertial attitude and angular velocity of the spacecraft are obtained through the inertial measurement unit and star sensor. The ACS with AFTC is a closed-loop system, as shown in Figure 1. An ASILO is responsible for giving an accurate estimate of the unknown lumped fault f, which can assist the RPP in adaptive adjustment and the controller in compensating for the fault. The red lightning symbol in the figure indicates potential faults of the actuators.

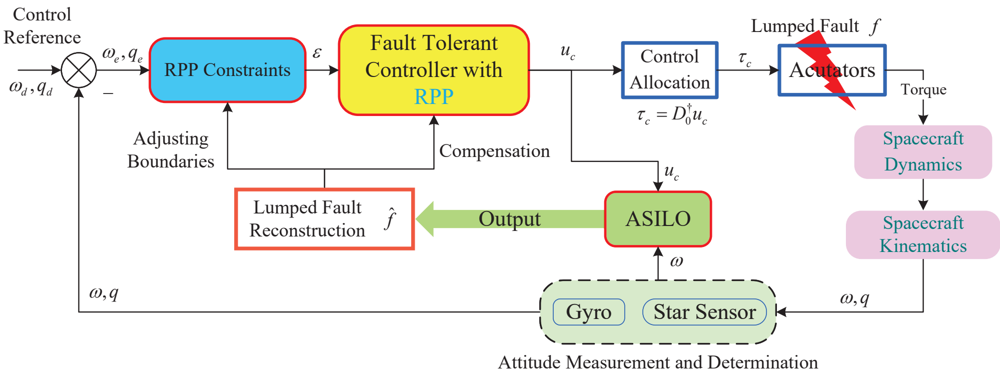

Figure 1. Spacecraft attitude control system with AFTC.

In order to accurately describe the attitude, it is necessary to define the inertial reference frame $\mathcal{I}$, the body fixed frame $\mathcal{B}$, and the desired attitude frame $\mathcal{D}$. To circumvent the singularity issues and reduce the computational complexity caused by the Euler angle description method, the attitude kinematics equation utilizing quaternions is presented as follows [47]:

$$\begin{cases} \dot{q}_0 = 0.5 \cdot q_v^{\mathrm{T}} \omega \\ \dot{q}_v = 0.5 \cdot (q_v^{\times} + q_0 I_3)\omega \end{cases} \tag{1}$$

where $q = [q_0, q_v^{\mathrm{T}}]^{\mathrm{T}} \in \mathbb{R}^{4\times1}$ is the unit quaternion obtained by the star sensor, which is used to describe the direction of the spacecraft $\mathcal{B}$ relative to $\mathcal{I}$. q_0 and q_v are the scalar part and vector part, respectively, and satisfy $\|q\|_2 = 1$. $\omega \in \mathbb{R}^{3\times1}$ is the angular velocity of $\mathcal{B}$ relative to $\mathcal{I}$ obtained by the IMU. $I_3 \in \mathbb{R}^{3\times3}$ is the identity matrix. $(\cdot)^{\times}$ is a corresponding skew-symmetric matrix expressed as

$$y = [y_1, y_2, y_3]^{\mathrm{T}}, y^{\times} = \begin{bmatrix} 0 & -y_3 & y_2 \\ y_3 & 0 & -y_1 \\ -y_2 & y_1 & 0 \end{bmatrix} \tag{2}$$

We assumed that the number of actuators was $n \geq 3$, and the spacecraft's dynamics can be given by

$$J_a \dot{\omega} = -\omega^{\times} J_a \omega + (D_0 + \Delta D)\tau_a + \tau_d \tag{3}$$

in which $J_a \in \mathbb{R}^{3\times3}$ is the actual moment of inertia matrix, including the nominal part J_0 and the uncertainty part ΔJ; $D_0 \in \mathbb{R}^{3\times n}$ is the nominal actuator configuration matrix and $\Delta D \in \mathbb{R}^{3\times n}$ is the error matrix; $\tau_a \in \mathbb{R}^{3\times1}$ is the actual output torque of the actuators; and $\tau_d \in \mathbb{R}^{3\times1}$ is the space environment disturbance torque suffered by the spacecraft, which mainly includes the gravity gradient torque, light pressure, and aerodynamic torque. Further considering the actuator faults and saturation, it can be expanded to

$$\tau_a = (I_n - \eta) \cdot \mathrm{sat}(\tau_c) + \tau_f \tag{4}$$

where τ_a and τ_c denote the actual control input and the control torque generated by the controller, respectively; $\eta = diag(\eta_1, \eta_2, \cdots \eta_n) \in \mathbb{R}^{n\times n}$ denotes the health loss matrix for actuators with $0 \leq \eta_i \leq 1, i = 1, 2, \cdots, n$, where $\eta_i = 1$ means that the i-th actuator is completely damaged and $\eta_i = 0$ means that the actuator is completely healthy; $\tau_f = [\tau_{f1}, \tau_{f1}, \cdots, \tau_{fn}]^T \in \mathbb{R}^{n\times 1}$ is the actuator bias fault; sat$(\cdot)$ represents the saturation constraint, which can be expressed as

$$\mathrm{sat}(\tau_c) = \begin{cases} \mathrm{sgn}(\tau_c)\cdot\tau_{\max}, & |\tau_{ci}| \geq \tau_{\max} \\ \tau_c, & |\tau_{ci}| < \tau_{\max} \end{cases}, i = 1, 2, \cdots, n \tag{5}$$

where $\mathrm{sgn}(\tau_c) = [sign(\tau_{c1}), sign(\tau_{c2}), \cdots, sign(\tau_{cn})]^{\mathrm{T}}$; and $\tau_{\max}$ is the maximum output capability of the actuators. Taking the above factors into account and substituting in (3), we obtain

$$\begin{aligned} &J_0\dot{\omega} = -\omega^\times J_0\omega + D_0\mathrm{sat}(\tau_c) + u_f + d \\ &d = J_0\tilde{J}[-\omega^\times J_a\omega + (D + \Delta D)\mathrm{sat}(\tau_c) + \tau_d + u_f] - \omega^\times \Delta J\omega + \tau_d + \Delta D\tau_a \end{aligned} \tag{6}$$

where $u_f = -D_0\eta\mathrm{sat}(\tau_c) + D_0\tau_f$, $\tilde{J} = -(J_0 + J_0\Delta J^{-1}J_0)^{-1}$, and $D_0\mathrm{sat}(\tau_c) = u_c$ denotes the control torque.

We let $f = u_f + d$ represent the lumped equivalent fault, including faults and uncertainties and disturbances other than the nominal model, to reduce the implementation complexity of the FDIR. To study the attitude-tracking problem, we define the error quaternion of $\mathcal{B}$ relative to $\mathcal{D}$ as $q_e = q_d^{-1} \odot q$; q_d is the desired attitude and $\odot$ represents the quaternion multiplication operation; and $\omega_e = \omega - C\omega_d$ represents the angular velocity error of $\mathcal{B}$ relative to $\mathcal{I}$, where ω_d is the desired angular velocity. $C = (q_{e0}^2 - q_{ev}^{\mathrm{T}}q_{ev})I_3 + 2q_{ev}q_{ev}^{\mathrm{T}} - 2q_{e0}q_{ev}^\times$ represents the corresponding rotation matrix between $\mathcal{B}$ and $\mathcal{D}$.

Control objectives: (1) Design a fault observer that can obtain the reconstruction of unknown actuator faults with a higher accuracy and speed to meet the requirements of FDIR. (2) Based on the obtained $\hat{f}$, improve the FTC with traditional PPC so that the ACS can prioritize stability when faults exist, addressing the control singularity issue. And enable q_e to always be strictly within the performance constraint.

Assumption 1. *q and ω can be obtained through star sensors and gyros. They are readily accessible for use in the design of observers and controllers in practice [40].*

Assumption 2. *The uncertainties ΔJ and ΔD, as well as the space environment disturbance τ_d and the actuator bias fault τ_f, are unknown but bounded [45,48,49]. This is due to the relatively high accuracy of the nominal model and the small amplitude of disturbance in practice, whereas actuator faults are unlikely to be unbounded due to physical energy constraints.*

Remark 1. *The method proposed in this paper is applicable under conditions where at least $\int_0^{t_1} f(t)dt \leq \int_0^{t_2} \mathrm{sgn}(f(t)) \cdot \tau_{\max}dt$ and $\int_0^{t_1}[\omega_0 + \int_0^{t_1} \frac{f_i(\delta)}{J_{ii}}d\delta]dt < \pi$, where t_1 should be small enough to ensure that there is always a suitable and acceptable t_2. Control systems with limited actuator capabilities can only handle bounded disturbances. This constraint states that the magnitude and duration of f cannot be infinite so that the resulting attitude deviation does not exceed 180°, and the resilient boundary is always less than 1. This is due to the property of q_e, which has no physical meaning when it exceeds 1. It can also be understood as a flight envelope. If this assumption does not hold, the method cannot guarantee its stability and may cause the system to diverge.*

3. Active Fault Tolerant Control Scheme Design

This section presents an improved AFTC scheme design method as shown in Figure 2, which mainly includes the ASILO to achieve fault reconstruction, laying a better foundation for FTC performance. Furthermore, FTC with RPP makes full use of fault information to reduce fault tolerance conservatism.

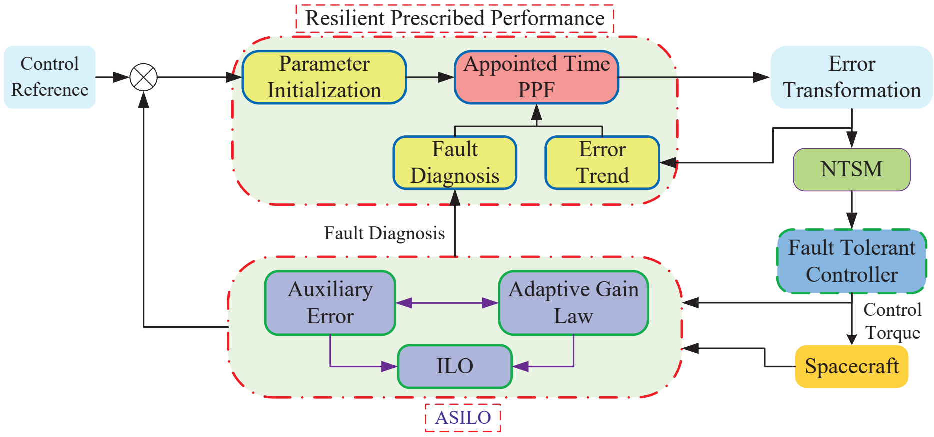

Figure 2. Improved AFTC scheme of spacecraft ACS.

3.1. Design of ASILO for Fault Reconstruction

This section presents a novel iterative learning observer based on auxiliary error and adaptive gain improvement to achieve an accurate reconstruction of the lumped equivalent fault f modeled in Section 2.

$$\begin{cases} J_0\dot{\hat{\omega}}(t) = -\hat{\omega}^{\times} J_0 \hat{\omega} + D_0 \mathrm{sat}(\tau_c(t)) + \hat{f}(t) + k_1\tilde{\omega}(t) + k_{s1}(s(t))\mathrm{sgn}[s(t)] \\ \hat{f}(t) = k_3\hat{f}(t-T) + k_4\tilde{\omega}(t) + k_{s2}(s(t))\mathrm{sgn}[s(t)] \end{cases} \tag{7}$$

where $t - T$ denotes the value of the variable in the previous learning cycle; T is the learning time interval of the ASILO; $\hat{\omega}(t)$ and $\hat{f}(t)$ represent the estimates of the angular velocity and lumped equivalent fault, respectively, where $\tilde{\omega}(t) = \omega(t) - \hat{\omega}(t)$ and $\tilde{f}(t) = f(t) - \hat{f}(t)$ are defined as their respective reconstruction errors; k_1, k_3, and k_4 are positive constant gains to be designed; $k_{s1}(s(t))$ and $k_{s2}(s(t))$ are the adaptive gains to be designed; and $s(t)$ is the fast-tracking auxiliary error to be designed, which has the following expression:

$$\begin{aligned} s(t) = & J_0\tilde{\omega}(t) - J_0\tilde{\omega}(0) + \int_0^t \omega^{\times}(\delta)J_0\omega(\delta) - \hat{\omega}^{\times}(\delta)J_0\hat{\omega}(\delta) \\ & + (k_1 + k_4)\tilde{\omega}(\delta) - k_3[f(\delta - T) - \hat{f}(\delta - T)]d\delta \end{aligned} \tag{8}$$

Since f in (8) cannot be obtained directly, we replace f with the fast estimated value $\overset{\frown}{f}$. With more accurate and directional error feedback from $\overset{\frown}{f}$, the iteration cycle can be reduced to a certain extent, thereby improving the convergence speed. $\overset{\frown}{f}$ can be obtained through

$$\overset{\frown}{f}(t) = \int_0^t -l \cdot [-\omega^{\times}(\delta)J_0\omega(\delta) + u_c(\delta) + \overset{\frown}{f}(\delta)]d\delta + l \cdot J_0\omega(t) \tag{9}$$

where l is the constant gain [50]. $\overset{\frown}{f}(t)$ is only a rough estimate, and its accuracy is less important, but its rapidity can help the error generated to guide the feedback correction to roughly point to the true value, rather than relying solely on the angular velocity estimation error iteration:

$$\begin{aligned} k_{s1}(t) = k_{s2}(t) = \frac{\alpha \underline{k}_s}{\alpha - \|s(t)\|}, \|s(t)\| \le \alpha - \frac{\alpha \underline{k}_s}{s_k} \\ \dot{k}_{s1}(t) = \dot{k}_{s2}(t) = k_a \|s(t)\|, \|s(t)\| > \alpha - \frac{\alpha \underline{k}_s}{s_k} \end{aligned} \tag{10}$$

in which $\underline{k}_s$ are the lower bounds of the adaptive gains $k_{s1}(t)$ and $k_{s,2}(t)$; when $\|s(t)\|= \alpha - \alpha\underline{k}_s/s_k$, $k_{s1}(t) = k_{s2}(t) = s_k$; and k_a is a positive scalar and can be chosen appropriately so that $\dot{k}_{s1}$ and $\dot{k}_{s2}$ remains continuous. α determines the changing rate of the adaptive gain. s_k represent the gain-switching threshold. This design ensures that $k_{s1}(t)$ and $k_{s2}(t)$ always remain continuous. Smaller α and s_k help improve the accuracy but slows down the speed. A smaller $\underline{k}_s$ generally results in a higher accuracy. But $\underline{k}_s$, α, and s_k still need to be appropriately designed according to performance requirements and stability requirements.

Assumption 3 ([19,22])**.** *In spacecraft engineering practice, as ω is a slowly varying component, it is reasonable to assume that $\dot{\omega}$ is always existent and bounded, and $\|\omega^\times(t)J_0\omega(t) - \hat{\omega}^\times(t)J_0\hat{\omega}(t)\| \le \gamma_\omega\|\tilde{\omega}\|$ holds for some known positive scalar γ_ω.*

Assumption 4 ([51])**.** *$f(t)$ is bounded and there exists $f(t) - k_3 f(t-T) \le \|f(t) - k_3 f(t-T)\| \le \sigma_{\max}$, where $\sigma_{\max}$ is a positive scalar.*

Lemma 1 ([52])**.** *Given the nonlinear system (7) with the sliding variable dynamics (8) controlled by (10), there exists a finite time $t_s > 0$ such that a real sliding mode is established, i.e., $\|s(t)\| < \alpha$, for $t > t_s$. And the gains $k_{s1}(t)$ and $k_{s2}(t)$ have an upper bound.*

Proof. To simplify the notation, (t) is omitted and the expression $(t-T)$ is replaced with $(\cdot)_{t-T}$. First, the convergence of the sliding mode surface $s(t)$ is proved. We design the Lyapunov function as

$$V_1 = \frac{1}{2}s^{\mathrm{T}}(t)s(t) + \frac{1}{2}[k_s(t,s(t)) - k^*]^{\mathrm{T}}[k_s(t,s(t)) - k^*] \tag{11}$$

where the lower bound of k_s is $\underline{k}_s$.

According to (6) and (7), we obtain

$$\dot{\tilde{\omega}} = J_0^{-1}[\hat{\omega}^\times J_0\hat{\omega} - \omega^\times J_0\omega - k_1\tilde{\omega} - k_{s1}\mathrm{sgn}(\tilde{\omega}) + f - \hat{f}] \tag{12}$$

Substitute $\hat{f}$ into the above equation to further obtain

$$\begin{aligned} \dot{\tilde{\omega}} = & -J_0^{-1}[k_1\tilde{\omega} + k_4\tilde{\omega} + k_{s1}\mathrm{sgn}(\tilde{\omega}) + k_{s2}\mathrm{sgn}(s) + (\omega^\times J_0\omega - \hat{\omega}J_0\hat{\omega}) \\ & - k_3\tilde{f}_{t-T} - (f - k_3 f_{t-T})] \end{aligned} \tag{13}$$

Take the derivative of (8):

$$\dot{s} = J_0\dot{\tilde{\omega}} + \omega^\times J_0\omega - \hat{\omega}^\times J_0\hat{\omega} + (k_1 + k_4)\tilde{\omega} - k_3\tilde{f}_{t-T} \tag{14}$$

Given (10), let $k_{s1} = k_{s2} = k_s$; then, we can have $\dot{k}_{s1} = \dot{k}_{s2} = \dot{k}_s$ and substitute (13) into the above equation:

$$\dot{s} = -k_{s1}\mathrm{sgn}(s) - k_{s2}\mathrm{sgn}(s) + (f - k_3 f_{t-T}) = -2k_s\mathrm{sgn}(s) + (f - k_3 f_{t-T}) \tag{15}$$

According to (10), it is not difficult to see that although the continuity of k_s is guaranteed, it still needs to be classified and discussed according to $\dot{k}_s$.

Case 1: When $\|s(t)\| \geq \alpha - \alpha \underline{k}_s / s_k$, that is, $\dot{k}_s = k_a \|s(t)\|$:

$$\begin{aligned} \dot{V}_1 &= s^{\mathrm{T}}[-2k_s \mathrm{sgn}(s) + (f - k_3 f_{t-T})] + (k_s - \underline{k}_s)\dot{k}_s \\ &\leq \sigma_{\max}\|s\| - 2k_s\|s\| + (k_s - \underline{k}_s)k_a\|s\| \\ &= -(2\underline{k}_s - \sigma_{\max})\|s\| - (2\|s\| - k_a\|s\|)(k_s - \underline{k}_s) \end{aligned} \tag{16}$$

There always exists a $\underline{k}_s > 0$ such that $\underline{k}_s - k_s < 0$ for all $t > 0$. To ensure stability, we need to make $\dot{V}_1 \leq 0$, so it is necessary to select appropriate parameters to make $\underline{k}_s \geq \frac{\sigma_{\max}}{2}$ and $0 < k_a < 2$ hold. This yields

$$\dot{V}_1 \leq -(2\underline{k}_s - \sigma_{\max})\|s\| - (k_a\|s\| - 2\|s\|)|\underline{k}_s - k_s| \tag{17}$$

Then, one obtains

$$\begin{aligned} \dot{V}_1 &\leq -(2\underline{k}_s - \sigma_{\max})\frac{\sqrt{2}\|s\|}{\sqrt{2}} - (2 - k_a)\|s\|\frac{\sqrt{2}|k_s - \underline{k}_s|}{\sqrt{2}} \\ &\leq -\min\{\sqrt{2}(2\underline{k}_s - \sigma_{\max}), \sqrt{2}(2\|s\| - k_a\|s\|)\}V_1^{\frac{1}{2}} \end{aligned} \tag{18}$$

Consider that when T is small enough, $\sigma_{\max}$ will also be a small positive scalar. To ensure that $\dot{V}_1$ is negative-definite, it is necessary to choose appropriate values for $\underline{k}_s$ and k_a such that $\underline{k}_s > 0.5\sigma_{\max}$ and $0 < k_a < 2$ hold. Therefore, according to Lemma 1, finite-time convergence to a neighborhood of $\|s(t)\| \leq \alpha$ is guaranteed from any initial condition within $t \leq 2\max\{V_1(0)\}^{1/2}/\sqrt{2}\min\{(2\underline{k}_s - \sigma_{\max}), (2\|s\| - k_a\|s\|)\}$.

Case 2: When $\|s(t)\| < \alpha - \alpha \underline{k}_s / s_k$. It is not difficult to obtain the following relationship through an appropriate transformation:

$$\begin{aligned} \dot{V}_1 &= s^{\mathrm{T}}(-2k_s \mathrm{sgn}(s) + f - k_3 f_{tT}) + (k_s - \underline{k}_s)\dot{k}_s \\ &\leq -(\frac{2\alpha \underset{\min}{\lambda}(k_s)}{\alpha - \|s\|} - \sigma_{\max})\|s\| - \frac{\alpha \underset{\min}{\lambda}(k_s)}{(\alpha - \|s\|)^2} \cdot \left| \frac{\alpha \underset{\min}{\lambda}(k_s)}{\alpha - \|s\|} - \underset{\min}{\lambda}(k_s) \right| \end{aligned} \tag{19}$$

where $\underset{\min}{\lambda}(k_s)$ represents the minimum eigenvalue of k_s. In order to simplify the expression process and increase the readability, we let $a = \frac{\alpha \underset{\min}{\lambda}(k_s)}{\alpha - \|s\|}$ and $b = \frac{\alpha \underset{\min}{\lambda}(k_s)}{(\alpha - \|s\|)^2}$. Then, $\dot{V}_1$ can be rewritten as

$$\begin{aligned} \dot{V}_1 &\leq -(a - \sigma_{\max})\|s\| - b \cdot \left| a - \underset{\min}{\lambda}(k_s) \right| \leq -\sqrt{2}\min\{a - \sigma_{\max}, b\}(\frac{\|s\|}{\sqrt{2}} + \frac{\left| a - \underset{\min}{\lambda}(k_s) \right|}{\sqrt{2}}) \\ &\leq -\sqrt{2}\min\{a - \sigma_{\max}, b\}V_1^{\frac{1}{2}} \end{aligned} \tag{20}$$

Since $b > 0$ holds, consequently, it is necessary to reasonably select appropriate parameters $\underline{k}_s$ so that $\frac{\alpha \underset{\min}{\lambda}(k_s)}{\alpha - \|s\|} \geq \underset{\min}{\lambda}(k_s) \geq \sigma_{\max}$, and we can obtain $a - \sigma_{\max} > 0$. Therefore, it is guaranteed that the auxiliary variable $s(t)$ can converge to the domain zero neighborhood within finite time $t \leq 2\max\{V_1(0)\}^{1/2}/\sqrt{2}\min\{(a - \sigma_{\max}), b\}$. Since $\underline{k}_s$ directly determines $\underset{\min}{\lambda}(k_s)$, selecting a larger $\underline{k}_s$ can shorten the convergence time. However, a too large $\underline{k}_s$ will cause chattering in the estimation and reduce the accuracy. We should choose a small $\underline{k}_s$ as much as possible while ensuring stability.

Next, the stability of the ASILO reconstruction errors also needs to be proved. The Lyapunov function is designed as $V_2 = \tilde{\omega}^{\mathrm{T}}(t)J_0\tilde{\omega} + \int_{t-T}^{t} \tilde{f}^{\mathrm{T}}(\delta)\tilde{f}(\delta)d\delta$. In the same way, by deriving V_2, we obtain

$$\dot{V}_2 = \tilde{\omega}^{\mathrm{T}}(t)J_0\dot{\tilde{\omega}}(t) + \tilde{f}^{\mathrm{T}}(t)\tilde{f}(t) - \tilde{f}^{\mathrm{T}}(t-T)\tilde{f}(t-T) \tag{21}$$

Since the convergence of $s(t)$ is proved above, there is a certain moment when $s(t)$ approaches the neighborhood of 0, and substituting into (8) produces

$$J_0\tilde{\omega}(t) - J_0\tilde{\omega}(0) + \int_0^t \hat{\omega}^{\times}J_0\hat{\omega} - \omega^{\times}J_0\omega + (k_1+k_4)\cdot\tilde{\omega}(\delta) - k_3[f(\delta-T) - \hat{f}(\delta-T)]d\delta = 0 \tag{22}$$

By deriving the above equation, we have

$$\dot{\tilde{\omega}} = J_0^{-1}[-\omega^{\times}J_0\omega + \hat{\omega}^{\times}J_0\hat{\omega} - (k_1+k_4)\tilde{\omega} - k_3\tilde{f}_{t-T}] \tag{23}$$

Resubstitute into (21):

$$\dot{V}_2 = -(k_1+k_4)\tilde{\omega}^{\mathrm{T}}\tilde{\omega} + \tilde{f}^{\mathrm{T}}\tilde{f} - \tilde{\omega}^{\mathrm{T}}(-\omega^{\times}J_0\omega + \hat{\omega}^{\times}J_0\hat{\omega}) - \tilde{\omega}^{\mathrm{T}}k_3{}^{\mathrm{T}}\tilde{f}_{t-T} - \tilde{f}_{t-T}^{\mathrm{T}}\tilde{f}_{t-T} \tag{24}$$

According to Young's inequality, there is the following relationship:

$$\begin{aligned} \tilde{f}^{\mathrm{T}}\tilde{f} &= \tilde{f}_{t-T}^{\mathrm{T}}k_3{}^{\mathrm{T}}k_3\tilde{f}_{t-T} + 2\tilde{f}_{t-T}^{\mathrm{T}}k_3{}^{\mathrm{T}}(f - k_3f_{t-T}) + (f - k_3f_{t-T})^{\mathrm{T}}(f - k_3f_{t-T}) \\ &\leq (1+\lambda_1)\tilde{f}_{t-T}^{\mathrm{T}}k_3{}^{\mathrm{T}}k_3\tilde{f}_{t-T} + (1+\frac{1}{\lambda_1})(f - k_3f_{t-T})^{\mathrm{T}}(f - k_3f_{t-T}) \end{aligned} \tag{25}$$

$$-\tilde{\omega}^{\mathrm{T}}k_3\tilde{f}_{t-T} \leq \lambda_2\tilde{\omega}^{\mathrm{T}}k_3{}^{\mathrm{T}}k_3\tilde{\omega} + \frac{1}{\lambda_2}\tilde{f}_{t-T}^{\mathrm{T}}\tilde{f}_{t-T} \tag{26}$$

where λ_1 and λ_2 are positive scalars from Young's inequality.

At the same time, there should be $\|\omega^{\times}J_0\omega - \hat{\omega}^{\times}J_0\hat{\omega}\| \leq \gamma_\omega\|\tilde{\omega}\|$. Therefore, by substituting all the above inequalities back into (24) and applying Young's inequality again gives

$$\begin{aligned} \dot{V}_2 \leq &-(\lambda_2\|k_3\|^2 + \|k_1+k_4\|^2 - \gamma_\omega)\|\tilde{\omega}\|^2 - [1 - \frac{1}{\lambda_2} - (1+\lambda_1)\cdot\|k_3\|^2]\|f_{t-T}\|^2 + \\ &(1+\kappa)(1+\frac{1}{\lambda_1})(f - k_3f_{t-T})^{\mathrm{T}}(f - k_3f_{t-T}) + \kappa(1+\lambda_1)\tilde{f}_{t-T}^{\mathrm{T}}k_3{}^{\mathrm{T}}k_3\tilde{f}_{t-T} - \kappa\|\tilde{f}\|^2 \end{aligned} \tag{27}$$

where κ is a positive scalar in Young's inequality.

By further manipulating the inequality and applying appropriate transformations, it is possible to derive

$$\begin{aligned} \dot{V}_2 \leq &-(\lambda_2\|k_3\|^2 + \|k_1+k_4\|^2 - \gamma_\omega)\|\tilde{\omega}\|^2 - [1 - \frac{1}{\lambda_2} - (1+\kappa)\cdot(1+\lambda_1)\|k_3\|^2]\cdot\|f_{t-T}\|^2 - \\ &\kappa\|\tilde{f}\|^2 + (1+\kappa)(1+\frac{1}{\lambda_1})\sigma_{\max}^2 \end{aligned} \tag{28}$$

Given $\lambda_1, \lambda_2, \kappa > 0$, to ensure negative-definiteness, it is not difficult to show that $1 - \frac{1}{\lambda_2} - (1+\kappa)\cdot(1+\lambda_1)\|k_3\|^2 > 0$ and $\lambda_2\|k_3\|^2 + \|k_1+k_4\|^2 - \gamma_\omega > 0$ should be established by selecting appropriate k_1, k_3, and k_4. In order to ensure the existence of solutions of k_3 and pursue higher performance and robustness, λ_1, λ_2, and κ should be selected to be large enough while at least satisfying $\lambda_2 > 1$. Considering that γ_ω is usually a very small value, it is easy to find the solutions of k_1, k_3, and k_4 when λ_2 is large enough. Given that V_2 satisfies stability when $\dot{V}_2 \leq 0$, it can be considered that the reconstruction error of the lumped fault $\tilde{f}$ will be less than $\|\tilde{f}\| \leq \sqrt{(1+\kappa)(1+\frac{1}{\lambda_1})\sigma_{\max}^2/\kappa}$. It is not difficult to see that the larger λ_1 and κ are, the smaller $\|\tilde{f}\|$ will be. On the other hand, the estimated error of ω will also satisfy

$$\|\tilde{\omega}\| \leq \sqrt{(1+\kappa)(1+\frac{1}{\lambda_1})\sigma_{\max}/(\lambda_2\|k_3\|^2 + \|k_1+k_4\|^2 - \gamma_\omega)}$$

After selecting the parameters that meet the above requirements, $\tilde{\omega}$ will obviously converge to a smaller error range. On the basis of satisfying the stability conditions, it is clear that selecting a larger k_1, k_3, and k_4 can help improve the reconstruction accuracy. However, the stability condition requires k_3 to be as small as possible, which creates a conflict with high performance. This necessitates a further trade-off with other parameters. □

3.2. Design of Resilient Prescribed Performance

The prescribed performance function (PPF) is a critical tool in PPC. It is used to constrain errors within desired performance specifications, directly influencing the overall control performance. The properties that the PPF $\rho(t)$ should meet include the following [40]:

1. $\rho(t)$ is smooth, positive, and at least first-order differentiable for all $t \geq 0$;
2. $\lim_{t\to 0}\rho(t) = \rho_0$, $\lim_{t\to\infty}\rho(t) = \rho_\infty$, and $\rho_0 > \rho_\infty > 0$.

The currently widely used PPF form is as follows [53]:

$$\rho(t) = (\rho_0 - \rho_\infty)e^{-kt} + \rho_\infty \tag{29}$$

where ρ_0 and ρ_∞ are the initial value and steady-state value of the PPF, respectively. k determines the convergence time. It lacks the capability to intuitively appoint a convergence time and does not ensure finite-time convergence. Notably, the adjustment of transient performance hinges solely on the parameter k, complicating its design significantly.

To address the aforementioned shortcomings of the traditional PPF, a novel design method for an appointed-time PPF is introduced here. Unlike the conventional approach detailed in (29), this new method ensures convergence within an appointed time.

$$\rho(t) = \begin{cases} x_1 + x_2 \cdot \sin(\frac{\pi t}{2t_f}) + x_3 \cdot \cos(\frac{\pi t}{2t_f}) + \frac{x_4}{\sinh(kt+b)}, & 0 \leq t \leq t_f \\ \rho_\infty, & t > t_f \end{cases} \tag{30}$$

where x_1, x_2, x_3, and x_4 are the parameters to be designed so that $\rho(t)$ satisfies the PPF property, and t_f represents the settable terminal time when $\rho(t)$ reaches ρ_∞. The boundary shape of the transient performance can be freely adjusted by adjusting k while keeping other parameters, such as t_f, unchanged, as shown in Figure 3. Users only need to specify $t_f, \rho_0, \rho_\infty, b$, and k in advance, and x_1, x_2, x_3, and x_4 can be automatically obtained according to (31). A larger ρ_0, ρ_∞, and t_f mean stronger robustness but also a lower accuracy.

$$\begin{aligned} x_4 &= \frac{\rho_0 - \rho_\infty}{\frac{k^2m^3 - 2k^2mn^2}{c^2m^4} - \frac{kn}{cm^2} + \frac{1}{\sinh(b)} - \frac{1}{m}}, \quad x_3 = -\frac{kn}{cm^2}x_4 \\ x_2 &= \frac{2k^2mn^2 - k^2m^3}{c^2m^4}x_4, \quad x_1 = \rho_0 - x_3 - \frac{1}{\sinh(b)}x_4 \end{aligned} \tag{31}$$

where $m = \sinh(kt_f + b), n = \cosh(kt_f + b)$, and $c = \pi/2t_f$; then, x_1, x_2, x_3, and x_4 can be obtained.

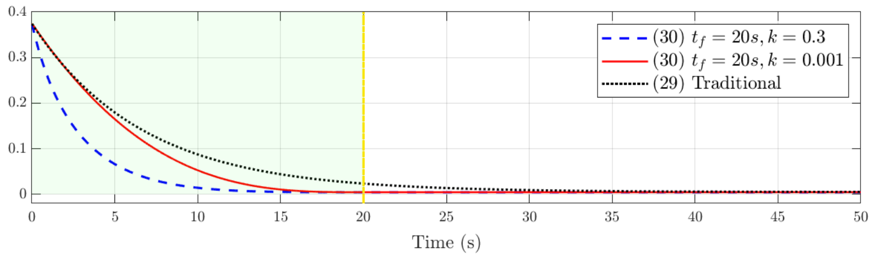

Figure 3. Comparison of PPF in (30) and (29).

Proof. The process of determining x_1, x_2, x_3, and x_4 is demonstrated by leveraging the fundamental properties of the PPF. We substitute (30) into the above properties to satisfy them, and we can obtain the following equation:

$$\rho(0) = \rho_0, \rho(t_f) = \rho_\infty, \lim_{t \to t_f^-} \dot{\rho}(t) = \lim_{t \to t_f^+} \dot{\rho}(t) = 0 \tag{32}$$

Further substituting the unknown parameters x_1, x_2, x_3, and x_4 into the above requirements yields

$$\begin{aligned} &x_1 + x_3 + x_4 \frac{1}{\sinh(b)} = \rho_0, \quad x_1 + x_2 + x_4 \frac{1}{m} = \rho_\infty \\ &- x_3 c - x_4 \frac{kn}{m^2} = 0, \quad -x_2 \cdot c^2 - x_4 \frac{k^2 m^3 - 2k^2 m n^2}{m^4} = 0 \end{aligned} \tag{33}$$

Since $m, n, c, \rho_\infty, \rho_0$, and k are known parameters, it is not difficult to simultaneously solve the aforementioned four equations, where the parameters x_1, x_2, x_3, and x_4 can be derived using the calculation method in (31). The parameter relationships designed through (31) ensure that the PPF possesses properties such as smoothness and differentiability. Proof complete. □

For the next step, based on the given appointed-time PPF in (30), the performance lower bound ρ_d and upper bound ρ_u of RPPF can be further designed as

$$\begin{cases} \rho_d(t) = [\mathrm{sgn}(e_0) - a]\rho(t) - \rho_\infty \mathrm{sgn}(e_0) - \psi_1(t) \\ \rho_u(t) = [\mathrm{sgn}(e_0) + a]\rho(t) - \rho_\infty \mathrm{sgn}(e_0) + \psi_2(t) \end{cases} \tag{34}$$

where e_0 is the initial value of the error, and a denotes the performance boundary shape parameter given by the user. Specifically, it should satisfy $\rho_d(t) < e(t) < \rho_u(t)$.

And $\psi_1(t)$ and $\psi_2(t)$ in (34) are the **resilient corrections** of $\rho_d(t)$ and $\rho_u(t)$, respectively, which are designed to handle error deviations caused by faults and avoid the control singularity for system stability. Inspired by [43], the design method of $\psi_1(t)$ and $\psi_2(t)$ can be described as

$$\begin{aligned} &\psi_1(t) = (1 - a) \cdot \varphi(t), \psi_2(t) = a \cdot \varphi(t) \\ &\varphi(t) = \tanh[\int_0^t [\frac{-\sigma_1 \varphi(\delta)}{|\varphi(\delta)| + \sigma_2} + \sigma_3 \Pi(\delta) + \sigma_4 \dot{\varepsilon}(\delta)] d\delta] \end{aligned} \tag{35}$$

in which $0 < a < 1$ is the correction coefficient, which determines the magnitude of resilient corrections; $\varphi(t)$ is the auxiliary variable, with its integral initial value $\varphi(0) = 0$; $\sigma_1, \sigma_2, \sigma_3$, and σ_4 are positive-definite gain parameters, where increasing σ_3 and σ_4 will extend the duration of the correction, while increasing σ_1 and σ_2 will shorten it; $\dot{\varepsilon}$ is the derivative of the transformed error introduced later; $\Pi(\delta)$ is the virtual control saturation, which can be given as follows:

$$\Pi(\delta) = u_c(\delta) - \text{sgn}(u_c(\delta)) \cdot \tau_{\max} \tag{36}$$

where $u_c(\cdot)$ is the control torque to be designed later; and $\tau_{\max}$ denotes the maximum output limit of the actuator. $-\sigma_1 \frac{\varphi(\delta)}{|\varphi(\delta)|+\sigma_2}$ in (35) is an attenuation term, which is used to restore the original constraint boundary after the fault is removed. $\sigma_3 \cdot \Pi(\delta)$ is the correction term caused by the actuator fault. And $\sigma_4 \cdot \dot{\varepsilon}(\delta)$ is the correction that is appropriately increased or decreased according to the error change trend. Through this design, the output saturation degree and the changing trend of the error caused by compensating for large-scale faults can be comprehensively sensed so as to make resilient corrections to $\rho_d(t)$ and $\rho_u(t)$ in a timely manner.

To enable the RPPF to handle arbitrary initial errors without the need for manual parameter adjustment across different scenarios, an automatic calculation mechanism for ρ_0, ρ_∞, and t_f is presented below:

$$\begin{aligned} \rho_0 &= c_1 \cdot \text{sgn}(q_{ev,i}) \cdot \max_{i=1,2,3}(|q_{ev,i}|) \\ \rho_\infty &= \max\{1, \left\| \hat{f}/\tau_{\max} \right\|_\infty\} \cdot \text{sgn}(q_{ev}) \cdot \rho_\infty \\ t_f &= \max_{i=1,2,3}\left[\sqrt{\frac{c_2 \pi}{180} \cdot \frac{4 \cdot \theta_i \cdot J_{ii}}{\tau_{\max} \cdot \left\| 1 - \left| \hat{f}/u_c \right| \right\|_\infty}} \right] \end{aligned} \tag{37}$$

in which c_1 and c_2 are amplification coefficients used to enhance the robustness; a larger c_1 and c_2 will result in better robustness but at the expense of the desired performance. θ_i is the Euler angle required for maneuvering along the i-th axis, and J_{ii} is the principal inertia of the i-th axis. Meanwhile, this mechanism introduces the physical meaning of the attitude control, making it more explainable in applications.

Remark 2. *The RPPFs given in (34) to (36) can achieve adaptive correction of the prescribed performance boundary based on fault diagnosis results, giving it a higher degree of application flexibility. The initialization calculation mechanism in (37) is used to solve the entry capture problem in traditional PPC, and will only act on the parameter initialization stage before the control starts, rather than the real-time effect during the control process. Therefore, it only involves the automatic initialization of parameters without affecting the stability.*

The comparison between traditional static PPF and RPP is demonstrated in Figure 4. The traditional static PPF in [53] does not have the ability to adjust online, causing the error to break through the boundary due to faults or disturbances, thereby leading to a control singularity. As is evident from Figure 5, the RPP can automatically initialize t_f, ρ_0, and ρ_∞ according to different initial scenarios with the help of the initialization mechanism before the control, which solves the entry capture problem and reduces the need for manual intervention.

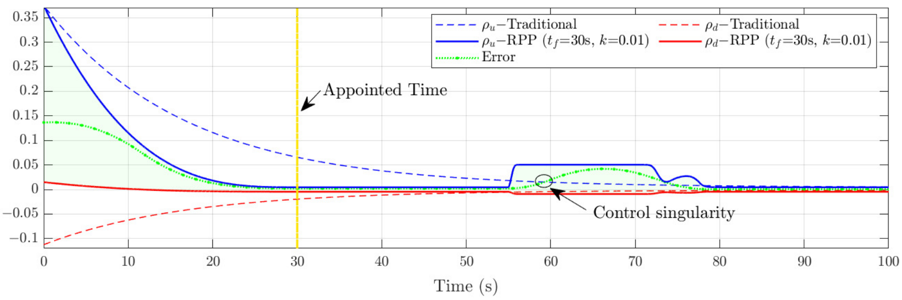

Figure 4. Comparison of static PPF in [53] and RPP.

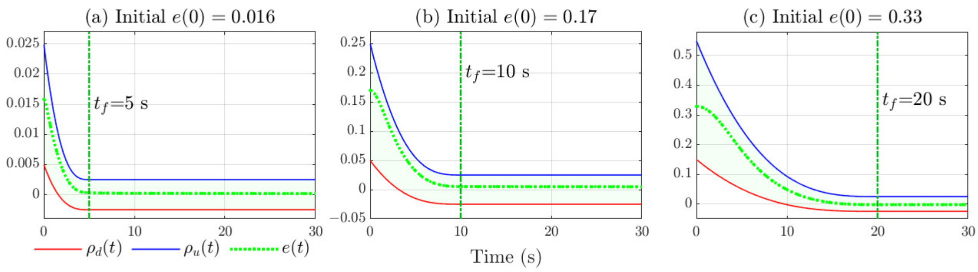

Figure 5. Initialization mechanism under different initial conditions.

3.3. Design of Fault-Tolerant Control with RPP

In order to make the attitude error quaternion remain in the predefined region, which satisfies $\rho_d(t) < q_{ev}(t) < \rho_u(t)$, there must also be $-\eta_{\min} < q_{ev} < \eta_{\max}$. It is necessary to further convert the constrained error into an equivalent unconstrained error through the error transformation $T(\cdot)$ [29].

Lemma 2 ([54]). *If the unconstrained error ε after the error transformation $T(\cdot)$ is bounded and converges, then it is equivalent to the constrained error q_{ev} converging and satisfying $\rho_d(t) < q_{ev}(t) < \rho_u(t)$. $T(\cdot)$ should satisfy the following:*

1. *$T(\cdot)$ is smooth and strictly monotonically increasing.*
2. *$\lim\limits_{\varepsilon\to+\infty} T^{-1}(q_{ev}) = \eta_{\max}$ and $\lim\limits_{\varepsilon\to-\infty} T^{-1}(q_{ev}) = -\eta_{\min}$, where $\rho_u(t) < \eta_{\max}$ and $-\eta_{\min} < \rho_d(t)$.*

To deal with such an issue, a function $T(\cdot)$ that satisfies the above conditions can be given as follows [36]:

$$\varepsilon(t) = T(q_{ev}(t)) = \ln\left(\frac{q_{ev}(t) - \rho_d(t)}{\rho_u(t) - q_{ev}(t)}\right) \tag{38}$$

where $\varepsilon(t)$ is the equivalent unconstrained error after transformation and $\dot{\varepsilon}(t)$ can be derived:

$$\dot{\varepsilon} = \frac{\rho_u - \rho_d}{(\rho_u - q_{ev})(q_{ev} - \rho_d)}[\dot{q}_{ev} + \frac{\rho_d\dot{\rho}_u - \dot{\rho}_d\rho_u + (\dot{\rho}_d - \dot{\rho}_u)q_{ev}}{\rho_u - \rho_d}] \tag{39}$$

for the convenience of writing, (t) is omitted hereafter. $\dot{\rho}_u$ and $\dot{\rho}_d$ can be obtained as

$$\begin{aligned} \dot{\rho}_d &= cx_2\cos(ct) - cx_3\sin(ct) - x_4\frac{k\cdot\cosh(kt+b)}{[\sinh(kt+b)]^2} - \dot{\psi}_1 \\ \dot{\rho}_u &= cx_2\cos(ct) - cx_3\sin(ct) - x_4\frac{k\cdot\cosh(kt+b)}{[\sinh(kt+b)]^2} + \dot{\psi}_2 \end{aligned} \tag{40}$$

Assumption 5. *Under all specified initial conditions, a feasible control strategy and corresponding parameters exist for the ACS [55] to achieve tracking control of a practical plant under input saturation under Assumptions 2 and 3. Users can test the applicability of this assumption through a reachability analysis [56].*

Remark 3. *Notably, an open-loop unstable system cannot be globally stabilized in the presence of input saturation. However, many practical plants always operate in some specified regions where they are controllable under the input saturation [57]. This is because the fault only lasts for a short time and the magnitude will not exceed the ACS's corrective capability. Control references are sent to the ACS only after strict pre-planning, and the spacecraft will not be operated outside the flight envelope.*

Based on the RPP, a class of active fault-tolerant controller is designed, and relevant theoretical proofs are given. Consider a nonsingular terminal sliding mode $s_2 \in R^{3\times 1}$ as $s_2 = \omega_e + \alpha_1 \varepsilon + \alpha_2 sig(\varepsilon)^r$, where $\alpha_1, \alpha_2 > 0, 0 < r < 1$, and $sig(\varepsilon)^r = \mathrm{diag}(\mathrm{sgn}(\varepsilon_i)|\varepsilon_i|^r)$. The time derivative of s_2 using (6) and (39) yields

$$J_0 \dot{s}_2 = J_0(\alpha_1 \dot{\varepsilon} + \dot{\omega}_e + \alpha_2 r S_\varepsilon \dot{\varepsilon}) = -\omega^\times J_0 \omega + u_c + f + J_0 \alpha_1 \dot{\varepsilon} + J_0 \alpha_2 r S_\varepsilon \dot{\varepsilon} \tag{41}$$

where $S_\varepsilon = \mathrm{diag}(|\varepsilon_i|^{r-1}),\ i = 1,2,3$. It should be pointed out that the computational cost of the improved RPP is almost equivalent to that of the traditional PPC. If the fault occurs before the original t_f is reached, the RPP will automatically adjust the boundary to cover the original t_f and constrain it according to the remaining performance after the fault.

Theorem 1. *The proposed fault-tolerant control law with RPP and sliding mode control can be designed as follows:*

$$u_c = \omega^\times J_0 \omega - J_0 \alpha_1 \dot{\varepsilon} - J_0 \alpha_2 r S_\varepsilon \dot{\varepsilon} - \alpha_3 s_2 - \alpha_4 sig(s_2)^r - \hat{f} \tag{42}$$

where α_3 and α_4 are positive-definite gain matrices.

The control law in (42) can make q_{ev} converge to the predefined steady-state accuracy with prescribed transient performance and ensure stability.

Proof. First, we demonstrate the stability of the sliding mode s_2, the Lyapunov function is selected as $V_3 = \frac{1}{2} s_2^{\mathrm{T}} J_0 s_2$, and its derivative $\dot{V}_3$ is

$$\dot{V}_3 = s_2^{\mathrm{T}}(-\omega^\times J_0 \omega + u_c + f + \alpha_1 J_0 \dot{\varepsilon} + \alpha_2 J_0 r S_\varepsilon \dot{\varepsilon}) \tag{43}$$

Substituting u_c from (42) into (43) and using the proven boundedness of $\tilde{f}$ gives

$$\begin{aligned} \dot{V}_3 &= s_2^{\mathrm{T}}(\tilde{f} - \alpha_3 s_2 - \alpha_4 sig(s_2)^r) \le \tilde{f}_m \|s_2\| - \alpha_3 \|s_2\|^2 - \|s_2\|^{\mathrm{T}} \alpha_4 \|s_2\|^r \\ &\le -\alpha_3 \|s_2\|^2 - (\|s_2\|^{\mathrm{T}} \alpha_4 \|s_2\|^{r-1} - \tilde{f}_m)\|s_2\| \end{aligned} \tag{44}$$

Since $\frac{1}{2} \underset{\min}{\lambda}(J_0)\|s_2\|^2 \le V_3 \le \frac{1}{2} \underset{\max}{\lambda}(J_0)\|s_2\|^2$ is established, it can be scaled to

$$\begin{aligned} \dot{V}_3 &\le \frac{-2\alpha_3}{\underset{\max}{\lambda}(J_0)} V_3 - (\|s_2\|^{\mathrm{T}} \alpha_4 \|s_2\|^{r-1} - \tilde{f}_m) \cdot \sum_{i=1}^{3} (\|s_{2i}\|^2)^{\frac{r+1}{2}} \\ &\le \frac{-2\alpha_3}{\underset{\max}{\lambda}(J_0)} V_3 - \frac{2^{\frac{r+1}{2}} (\|s_2\|^{\mathrm{T}} \alpha_4 \|s_2\|^{r-1} - \tilde{f}_m)}{\underset{\max}{\lambda}(J_0)^{\frac{r+1}{2}}} \cdot V_3^{\frac{r+1}{2}} \end{aligned} \tag{45}$$

Since $\alpha_3, \alpha_4 > 0$, and $\underset{\min}{\lambda}(J_0), \underset{\max}{\lambda}(J_0) > 0$, we need to make $\|s\|^{\mathrm{T}} \alpha_4 \|s\|^{r-1} - \tilde{f}_m = K > 0$ to ensure $\dot{V}_3 \le 0$. Since $\tilde{f}_m$ can be sufficiently small, it is necessary to select an appropriate and sufficiently large α_4 to ensure that $K > 0$. And the larger the α_3 and α_4 are, the faster the convergence speed will be. However, if α_3 is too large, the actuator will be oversaturated and the overshoot will increase, and if α_4 is too large, it will cause chattering. It is necessary to select appropriately according to the performance requirements. Then, the real sliding mode can reach the neighborhood of 0 within a finite time, and the time satisfies

$$T \le \frac{\underset{\max}{\lambda}(J_0)}{\alpha_3(1-r)} \ln \frac{\frac{2\alpha_3 V_3^{(1-r)/2}}{\underset{\max}{\lambda}(J_0)} + \frac{2^{(1+r)/2} K}{\underset{\max}{\lambda}(J_0)^{(1+r)/2}}}{2^{(1+r)/2} K / \underset{\max}{\lambda}(J_0)^{(1+r)/2}}$$

We further prove the stability of q_e as s approaches 0. Consider the following new Lyapunov function $V_4 = \frac{1}{2}\varepsilon^{\mathrm{T}}\varepsilon$. Since there are no potential discontinuities, it is only necessary to analyze according to the continuous system. Taking its derivative, we obtain

$$\dot{V}_4 = \varepsilon^{\mathrm{T}}\dot{\varepsilon} = \varepsilon^{\mathrm{T}}\frac{\rho_u - \rho_d}{(\rho_u - q_{ev})(q_{ev} - \rho_d)}[\dot{q}_{ev} + \frac{\rho_d\dot{\rho}_u - \dot{\rho}_d\rho_u + (\dot{\rho}_d - \dot{\rho}_u)q_{ev}}{\rho_u - \rho_d}] \tag{46}$$

When $s \to 0$, there exists $\omega_e = -\alpha_1\varepsilon - \alpha_2 sig(\varepsilon)^r$, and substituting in (39), we obtain

$$\begin{aligned}\dot{V}_4 = \varepsilon^{\mathrm{T}}&\frac{\rho_u - \rho_d}{(\rho_u - q_{ev})(q_{ev} - \rho_d)}[-\alpha_1 Q\varepsilon - \alpha_2 Q sig(\varepsilon)^r + \frac{\rho_d\dot{\rho}_u - \dot{\rho}_d\rho_u}{\rho_u - \rho_d} + \\ &\frac{\dot{\rho}_d - \dot{\rho}_u}{\rho_u - \rho_d}\cdot\frac{e^{\varepsilon}\rho_u + \rho_d}{1 + e^{\varepsilon}}]\end{aligned} \tag{47}$$

Let $\frac{\rho_u - \rho_d}{(\rho_u - q_{ev})(q_{ev} - \rho_d)} = M$. Based on the design principles of ρ and φ and properties such as $\rho_u > \rho_d > 0$, $\dot{\rho} < 0$, $0 < \varphi$, and $\dot{\varphi} < 1$, where they are all bounded, it is not difficult to deduce that the following relationships hold:

$$\begin{aligned}\frac{\rho_d\dot{\rho}_u - \dot{\rho}_d\rho_u}{\rho_u - \rho_d} &= \frac{-2a\dot{\rho}\rho_\infty - (a - 2a^2 - 1)(\dot{\rho}\varphi - \rho\dot{\varphi}) - \rho_\infty\dot{\varphi}}{2a\rho + \varphi} \le \frac{-2a\dot{\rho}\rho_\infty}{2a\rho_0} \le \tilde{\rho}_1\rho_\infty \\ \frac{\dot{\rho}_d - \dot{\rho}_u}{\rho_u - \rho_d} &= \frac{-2a\dot{\rho} - \dot{\varphi}}{2a\rho + \varphi} \le \frac{-2a\dot{\rho}}{2a\rho + 1} \le \tilde{\rho}_2 \\ \frac{e^{\varepsilon}\rho_u + \rho_d}{1 + e^{\varepsilon}} &= \rho_u - \frac{\rho_u - \rho_d}{1 + e^{\varepsilon}} < \rho_u\end{aligned} \tag{48}$$

where $\tilde{\rho}_1$ and $\tilde{\rho}_2$ are known positive scalars; $\tilde{\rho}_1$ and $\tilde{\rho}_2$ can usually be made sufficiently small by a high-precision ρ design. $a - 2a^2 - 1 < 0$ because $0 < a < 1$, $\dot{\rho}\varphi - \rho\dot{\varphi} < 0$, and $\rho_\infty\dot{\varphi} > 0$. And we can further derive

$$\begin{aligned}\dot{V}_4 \le& -\varepsilon^{\mathrm{T}}M\alpha_1 Q\varepsilon - \varepsilon^{\mathrm{T}}M\alpha_2 Q sig(\varepsilon)^r + \varepsilon^{\mathrm{T}}M\frac{\rho_d\dot{\rho}_u - \dot{\rho}_d\rho_u}{\rho_u - \rho_d} + \varepsilon^T M\frac{(\dot{\rho}_d - \dot{\rho}_u)\rho_u}{\rho_u - \rho_d} \\ \le& -\varepsilon^{\mathrm{T}}M\alpha_1 Q\varepsilon - \varepsilon^{\mathrm{T}}M\alpha_2 Q sig(\varepsilon)^r + \tilde{\rho}_1\rho_\infty\varepsilon^T M + \tilde{\rho}_2((1 + a)\rho_0 + \rho_\infty + a)\varepsilon^T M\end{aligned} \tag{49}$$

The positive-definiteness of Q can refer to the minor values, which are $\frac{1}{2}q_0, q_0^2 + q_3^2$, and q_0, so we need to further discuss the sign of q_0. Considering that in actual engineering, in order to prevent the attitude unwinding phenomenon and maintain the uniqueness of attitude instructions and the stability of numerical calculations on board, the parameter $q_0 > 0$ should be selected in the dual quaternion for instruction planning so that the positive definiteness of Q can always be satisfied. Since the unit quaternion q is defined to satisfy $q_0^2 + q_1^2 + q_2^2 + q_3^2 = 1, 0 \le q_i \le 1$, we have $\|Q\| < 1$. Furthermore, according to Young's inequality, we can derive that

$$\begin{aligned}\dot{V}_4 \le& -(\alpha_1 - \gamma_1\tilde{\rho}_1\rho_\infty)\|M\|\|\varepsilon\|^2 - \alpha_2\|M\|\|\varepsilon\|^{r+1} + \frac{\tilde{\rho}_1\rho_\infty}{\gamma_1} + \frac{\tilde{\rho}_2((1 + a)\rho_0 + \rho_\infty + a)}{\gamma_2} \\ \le& -(\alpha_1 - \gamma_1\tilde{\rho}_1\rho_\infty)\|M\|V_4 - \alpha_2\|M\|V_4^{\frac{r+1}{2}} + \frac{\tilde{\rho}_1\rho_\infty}{\gamma_1} + \frac{\tilde{\rho}_2((1 + a)\rho_0 + \rho_\infty + a)}{\gamma_2}\end{aligned} \tag{50}$$

where γ_1 and γ_2 are positive scalars from Young's inequality. In order to ensure the negative-definiteness of $\dot{V}_4$, appropriate $\alpha_1, \alpha_2 > 0$ and $\gamma_1, \gamma_2 > 0$ should be selected to ensure the existence of the solution. First, α_1 should be chosen to be large enough so that $\alpha_1 > \gamma_1\tilde{\rho}_1\rho_\infty$ is satisfied. According to the properties of ρ and q_e, $\|M\| \le \tilde{\rho}_m$ exists. It should be pointed out that $a, \tilde{\rho}_1$, and $\tilde{\rho}_2$ are directly related to the resilient boundary. Although it is difficult to directly give an explicit mathematical relationship between them, their association is guaranteed by the effective and reasonable designs of (35) and (37).

After the stability conditions are met, it is not difficult to analyze that V_4 will converge to an error range within a finite time:

$$T \leq \frac{\ln(1+\frac{\alpha_1-\gamma_1\tilde{\rho}_1\rho_\infty}{\alpha_2}V_4^{\frac{1-r}{2}}(0))}{(\alpha_1-\gamma_1\tilde{\rho}_1\rho_\infty)(1-r)}, \|\varepsilon\| \leq \sqrt{\frac{2\tilde{\rho}_1\rho_\infty\gamma_2+2\tilde{\rho}_2\gamma_1((1+a)\rho_0+\rho_\infty+a)}{(\alpha_1-\gamma_1\tilde{\rho}_1\rho_\infty)\gamma_1\gamma_2\tilde{\rho}_m}}$$

According to the above discussion, selecting a larger γ_1 andγ_2 and smaller a, ρ_∞, and ρ_0 will help improve the convergence accuracy, and a larger α_2 will help improve the convergence speed. This is also consistent with the design intuition of ρ_u and ρ_d mentioned earlier, as tighter performance boundaries and resilient corrections imply a higher accuracy. By selecting a larger a, it can be ensured that q_{ev} is always between ρ_u and ρ_d when a fault exists, thereby ensuring stability. However, if a, ρ_∞, and ρ_0 are too large, the resilient correction will not match the actual demand, resulting in excessive conservatism. It should be noted that as γ_1 increases, α_1 should also increase. However, if α_1 is too large, the overshoot will increase, and if α_2 is too large, it will cause chattering in the control. So the parameters should be appropriate and balanced while ensuring stability. According to Lemma 2, if the stability of ε is satisfied, it is equivalent to q_{ev} ensuring stability while satisfying the constraints of the specified performance. The stability is ensured by introducing a resilient trade-off between the fault and performance. The sufficient condition for obtaining steady-state accurate tracking is

$$\mathcal{P} := \{(t, \omega_d(t)) : t \in R_+, \frac{|J_0\dot{\omega}_d + \omega^\times J_0\omega - f|}{D_0} < \tau_{\max}\}$$

When the control torque reaches saturation, the influence of the fault deviation on the system stability is corrected by the resilient boundary, so it can be concluded that

$$\dot{V}_3 = s_2^{\mathrm{T}} J_0(-\omega^\times J_0\omega - \tau_{\max} + d + \alpha_1\dot{\varepsilon} + \alpha_2 r S_\varepsilon \dot{\varepsilon})$$

At the same time, according to the above discussion, there is $\|-\omega^\times J_0\omega\| \leq J_0\|\omega\|^2$, $\|\alpha_1\dot{\varepsilon} + \alpha_2 r S_\varepsilon\dot{\varepsilon}\| \leq (\alpha_1 + \alpha_2 r\tilde{S}_\varepsilon)(\tilde{\rho}_1\rho_\infty + \tilde{\rho}_2\rho_u)$. To ensure stability, $\tau_{\max} \geq J_0\|\omega\|^2 + (\alpha_1 + \alpha_2 r\tilde{S}_\varepsilon)(\tilde{\rho}_1\rho_\infty + \tilde{\rho}_2\rho_u) + \|d\|$ should also be established at the beginning of the spacecraft design [58]. □

Remark 4. *The initialization mechanism only involves the automatic adjustment of the initial parameters, which is used to replace the manual assignment before the PPC starts. It does not directly participate in the control and affect stability. On the other hand, when a fault that satisfies Assumption 3 temporarily (briefly) exceeds the actuator's compensation range, resilient correction is deployed by broadening the performance boundary to temporarily accommodate the increased error and avoid a control singularity. Stability during this phase is guaranteed by a well-designed resilient boundary rather than the control law itself. As long as the resilient boundary can always contain the error during the fault, a control singularity can be avoided. After the fault weakens or disappears, it will return to normal PPC, and stability will be guaranteed by the control law again. The results regarding the stability properties under saturation are expected to be local.*

4. Simulation Results

In order to verify the effectiveness and performance of the AFTC method proposed in this article, this section presents numerical simulation experiments and corresponding comparisons for rigid spacecraft ACS. The simulation software uses MATLAB 2018a.

In the numerical simulation, it was assumed that the nominal moment of inertia matrix J of the spacecraft and its uncertainty ΔJ were respectively set as

$$J_0 = \begin{bmatrix} 89 & 0.2 & 1.5 \\ 0.2 & 61 & 0.7 \\ 1.5 & 0.7 & 57 \end{bmatrix} \mathrm{kg} \cdot \mathrm{m}^2, \Delta J = 0.02 \cdot J_0 \quad (51)$$

The spacecraft ACS adopted a common four-redundant configuration. The actuator configuration matrix and its error matrix were set to $D_0 = \begin{bmatrix} I_{3\times3} & [1/\sqrt{3}, 1/\sqrt{3}, 1/\sqrt{3}]^{\mathrm{T}} \end{bmatrix}$ and $\Delta D = 0.001 \cdot D_0$, respectively. The maximum output torque capacity of a single actuator was 0.2 N · m. The fault scenarios of three RWs are specifically described in Figure 6, where green means that the actuator has no fault, and the closer the color is to red, the more serious the fault scale is.

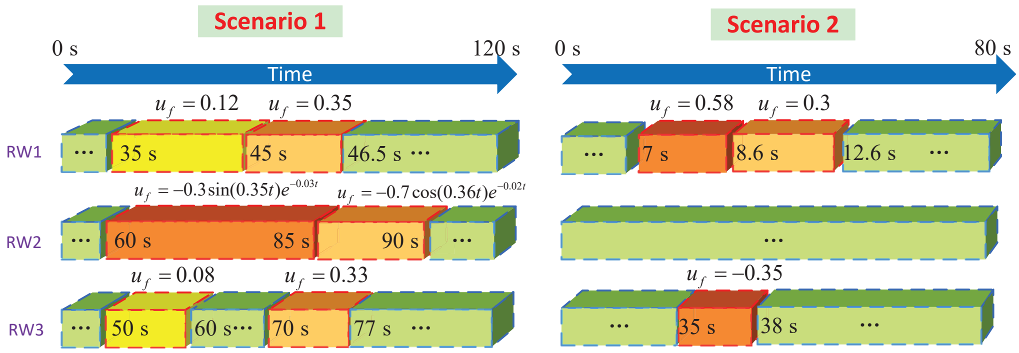

Figure 6. Different actuator faults scenarios.

Corresponding to Figure 6, the following formulas give specific expressions of the faults of different actuators:

$$\begin{aligned} &Scenario\ 1: \\ &u_{f_1} = \begin{cases} 0.12, & 35 \le t < 45 \\ 0.35, & 45 \le t < 46.5 \\ 0, & else \end{cases}, u_{f_2} = \begin{cases} -0.3\sin(0.35t)e^{-0.03t}, & 60 \le t < 85 \\ -0.7\cos(0.36t)e^{-0.02t}, & 85 \le t < 90 \\ 0, & else \end{cases}, u_{f_3} = \begin{cases} 0.08, & 50 \le t < 60 \\ 0.33, & 70 \le t < 77 \\ 0, & else \end{cases} \\ &Scenario\ 2: \\ &u_{f_1} = \begin{cases} 0.58, & 7 \le t < 8.6 \\ 0.3, & 8.6 \le t < 12.6 \\ 0, & else \end{cases}, u_{f_2} = 0,\ u_{f_3} = \begin{cases} -0.35, & 35 \le t < 38 \\ 0, & else \end{cases} \end{aligned} \quad (52)$$

The specific expressions of the faults given in (52) were divided into Scenarios 1 and 2. They were composed of abrupt, time-varying, and intermittent faults. The corresponding physical meaning mainly included unpredictable short circuits, damage, performance degradation, parameter drifts, and poor contacts [59]. This design was to better test the rapidity of the ASILO in estimating abrupt faults and the accuracy of time-varying faults. It included a large number of faults that exceeded the output capacity of the actuator, which verified the excellent fault tolerance performance of the RPP and could solve the fault scenarios that the PPC could not handle.

To ensure the applicability of the proposed method, all faults in the scenario satisfied Assumptions 2, 3, and 6. And the space environment disturbances were selected as $\tau_d = [\tau_{droll}, \tau_{dpitch}, \tau_{dyaw}]^T + v_d$:

$$\begin{aligned} \tau_{droll} &= 0.005\sin(0.15t)\cos(0.05t) + 0.002\cos(0.65t) \\ \tau_{dpitch} &= 0.01\cos(0.33t)\cos(0.22t) + 0.001\cos(0.33t) \\ \tau_{dyaw} &= 0.002\sin(0.08t)\sin(0.35t) + 0.003\cos(0.22t) \end{aligned} \tag{53}$$

where v_d is colored noise used to represent unmodeled factors, such as spacecraft micro-vibration.

After the equivalent transformation of (3)–(6), the lumped equivalent fault f, including the uncertainty, disturbance, and fault, is shown more intuitively and clearly in Figure 7, which is used to verify the performance improvement of the ASILO in the fault reconstruction. And the main design parameters of ASILO were selected as $k_1 = diag(420, 420, 420), k_3 = diag(1, 1, 1)$, $k_4 = diag(70, 70, 70)$, $k_a = 1.2$, $\alpha = 0.1$, $s_k = 0.00104$, and $\underline{k}_s = 0.0001$.

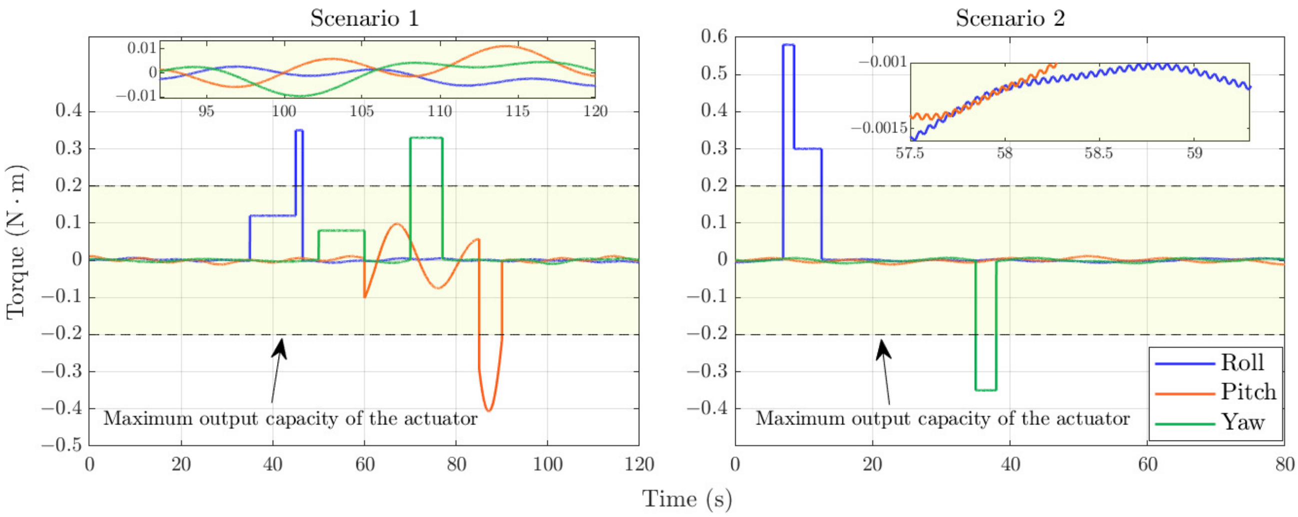

Figure 7. Lumped equivalent fault f scenarios.

First, the effectiveness of the fault reconstruction method based on the ASILO proposed in this paper was verified. The comparison methods were the traditional ILO, AILO, STCKF, and ASILO. As shown in Figures 8 and 9, the traditional ILO suffered from a slow convergence and low accuracy. Its convergence speed failed to meet the fault diagnosis requirements, and its accuracy was insufficient for the AFTC design. The AILO introduced an adaptive gain adjustment mechanism, which improved both the convergence speed and accuracy, though still with room for improvement. In contrast, combined with strong tracking algorithms, the STCKF significantly enhanced the estimation speed and accuracy. As shown in Figure 8, the STCKF met the fault diagnosis performance requirements, but at the cost of higher computational demands, which strained the spacecraft hardware resources. The fault reconstruction performance was evaluated through the following indicators:

1. Accuracy, using the root-mean-square error (RMSE) as the measurement index. The smaller the RMSE, the higher the reconstruction accuracy.
2. Rapidity, defined by how quickly an estimation converged to within a 5% error margin of the true value. The shorter the time, the greater the rapidity.
3. Complexity, as measured by the calculation time under the same experimental conditions. The shorter the time, the less computational resources were consumed.

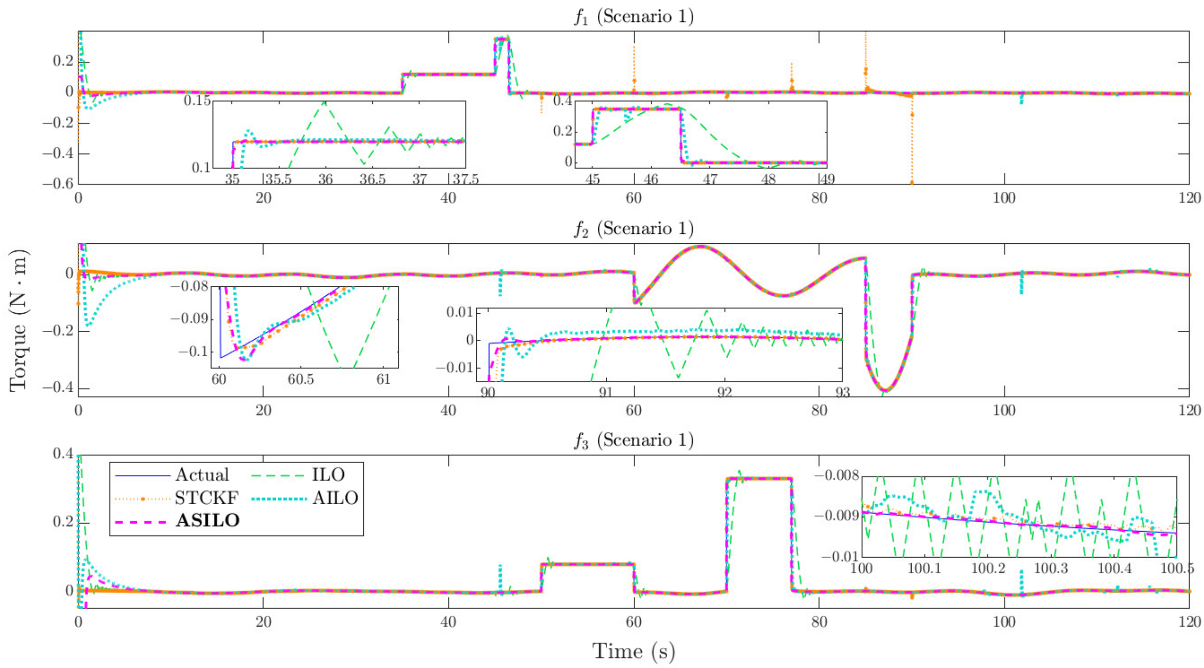

Figure 8. Fault reconstruction $\hat{f}$ in Scenario 1 based on different methods.

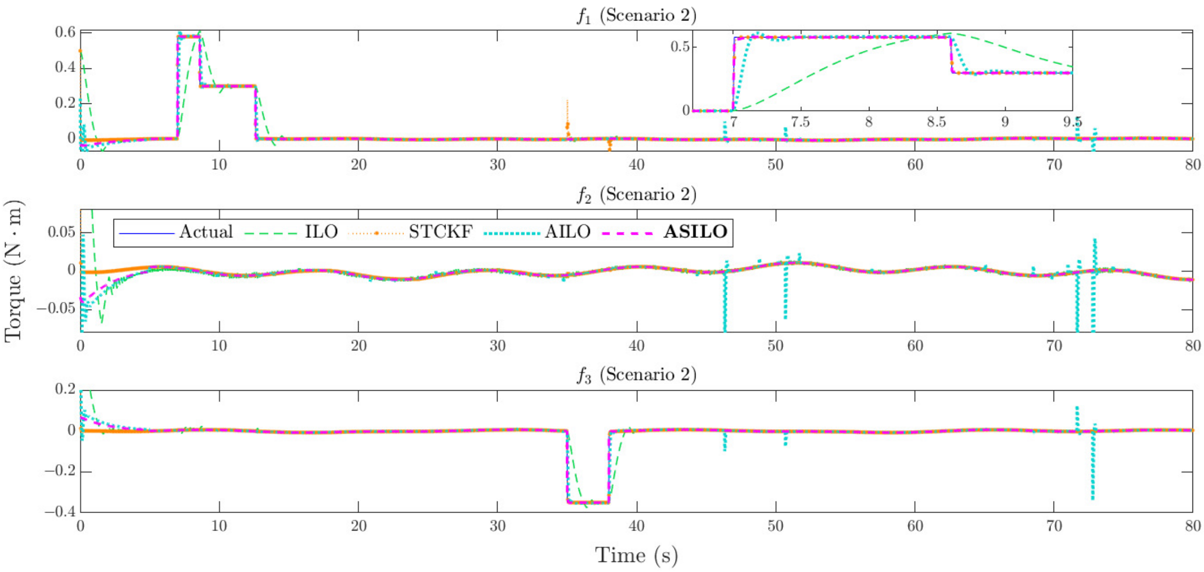

Figure 9. Fault reconstruction $\hat{f}$ in Scenario 2 based on different methods.

Furthermore, the fault reconstruction based on the ASILO can be found in Figures 8 and 9. It can be seen from this that by introducing an auxiliary error and adaptive gain, the ASILO was better than the ILO and AILO in terms of the convergence speed and accuracy. It could achieve better performance indicators for both the mutation faults and slowly changing faults. Table 1 demonstrates the specific fault-reconstruction performance index comparison of the four different methods given through quantitative expression. The ASILO and STCKF achieved similar accuracies, but the STCKF converged faster. It should be pointed out that the STCKF's excellent speed needs powerful computing resources. On spacecraft platforms with scarce computing resources, the ASILO can use a small amount of operation close to the traditional ILO to achieve a better speed while remaining able to meet the rapidity of fault diagnosis requirements. In addition, in order to more intuitively demonstrate how the design parameters in the ASILO affect its performance, we briefly compared the accuracy and rapidity under different parameters. When $\underline{k}_s$ increased to 0.005 and 0.01, the RMSE increased to 8.677×10^{-4} and 2.652×10^{-3}, respectively. Although the rapidity changed to 0.352 s and 0.348 s, the improvement was very limited. Reducing k_1 reduced the accuracy. For example, when $k_1 = 20$, the RMSE increased to 0.0042. Similarly, reducing k_4 reduced the rapidity. For example, when $k_4 = 30$, the rapidity increased to 0.73 s. However, any value of k_4 led to repeated over-regulation, which was detrimental to the performance. The influence of k_3 was more complex and coupled, so, for example, when $k_3 = 0.8$, the RMSE increased sharply to 0.011. When $k_3 > 1$, stability may not be achieved.

Table 1. Comparison of fault reconstruction performances.

Method	Accuracy	Rapidity	Complexity
ILO	0.0015	2.015 s	0.8353 s
AILO	7.763×10^{-4}	0.754 s	0.9127 s
STCKF	5.218×10^{-4}	0.121 s	4.4457 s
ASILO	4.985×10^{-4}	0.358 s	1.0421 s

In order to verify the adaptability of the initialization mechanism in the RPP to different initial errors, different initial errors were given for Scenarios 1 and 2. The initial attitude of Scenario 1 was $[16°, 3°, 22°]$, and the maneuver command was $[0°, -3\cos(0.05t)°, -10°]$. The initial attitude of Scenario 2 was $[-0.004°, -3°, -0.003°]$, and the maneuver command was $[-5°, -10°, -6°]$. The main parameters in the RPP were chosen as $a = 0.9$, $c_1 = 2.1$, $c_2 = 1.6$, $\sigma_1 = 7$, $\sigma_2 = 2$, $\sigma_3 = 0.7$, and $\sigma_4 = 0.5$. And the parameters in the control law were selected as $\alpha_1 = 0.12$, $\alpha_2 = 0.3$, $r = 1.4$, $\alpha_3 = 0.1$, and $\alpha_4 = 0.002$.

In order to demonstrate the superiority of the AFTC scheme with the RPP proposed in this paper, first, Figure 10 demonstrates the RPP with no fault. We can see that under fault-free conditions, even after adding the disturbance, the performance shown in Figure 10 does not change at all. The RPP could perform well under performance constraints regardless of whether there was a disturbance. This was because the disturbances were usually very small and it was difficult to produce saturation without the intervention of a resilient correction. Since the actuator had no fault, the resilient correction was not effective at this time, which can be regarded as the traditional appointed-time PPC. The quaternion error q_{ev} could converge to the desired accuracy within the specified time. There was no control singularity problem. However, when the actuator fails, if the performance boundary remains static, the error will inevitably exceed the boundary, causing a control singularity and failure to ensure system stability.

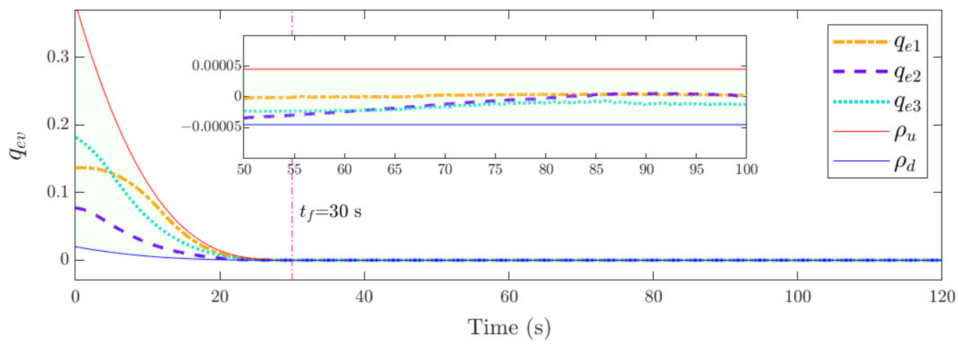

Figure 10. Time response of q_e under RPP without faults.

The core idea of the RPP is to temporarily compromise performance constraints in exchange for control stability when encountering large-scale faults, which can be called "resilient prescribed performance". As shown in Figure 11, the AFTC with the RPP had the ability to adaptively adjust according to actuator faults during the control process. The RPP made corresponding boundary corrections for the fault sets in Scenarios 1 and 2. When the actuator could not completely offset the trajectory deviation caused by the fault, it actively relaxed the boundary to ensure that $\rho_d < q_e < \rho_u$ could always be satisfied, which ensured the stability of the PPC and avoided a control singularity. When the fault weakened or disappeared, the resilient correction gradually became smaller, which narrowed the boundary again to promote its return to the expected performance. This greatly reduced the conservatism of the PPC when used for the FTC. On the other hand, the different initial conditions of Scenarios 1 and 2 also verified the effectiveness of the initialization mechanism in the RPP. Due to the inherent nature of PPC, it is necessary to manually assign parameters, such as ρ_0, ρ_∞, and t_f, before each control to ensure that the initial error does not fall outside the performance boundary. This tedious work restricts the universality of PPC. However, the initialization mechanism combines the physical behavior of the spacecraft ACS to provide an automated parameter initialization method to solve the entry capture problem. While avoiding the initial error falling outside the performance boundary, it also avoids manual intervention and improves the universality. On the other hand, the RPP can also automatically cover the t_f that was originally specified but cannot be realized due to the fault, and thus, achieve the control target through resilient boundaries. This avoids a control singularity caused by sticking to a user-specified t_f.

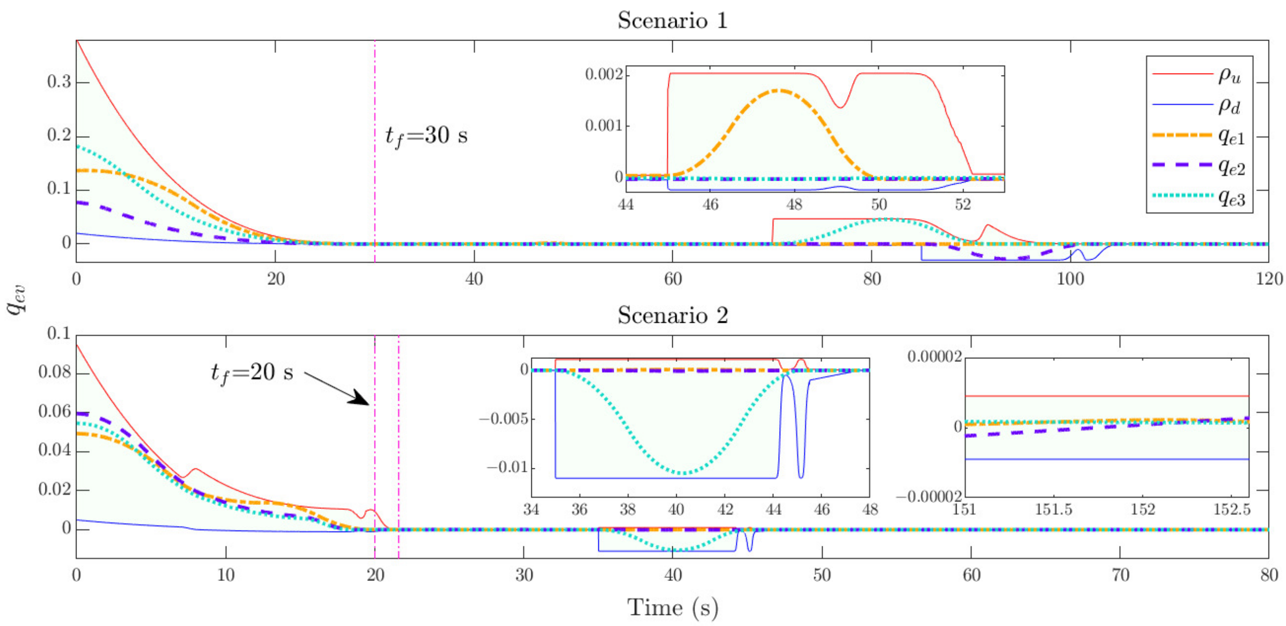

Figure 11. Time response of q_e under AFTC with RPP.

As a comparison, the experimental results based on existing methods are given in Figure 12, including the FTC based on the traditional static PPC and the adaptive PPC proposed in [43]. Figure 12a shows the AFTC based on a traditional static PPC design, which does not include any performance boundary adjustment mechanism. The green area in the figure represents the hypothetical prescribed performance constraints, which is the same as the green area in Figure 11. It is not difficult to see that even if the actuator fault was not large enough, the error fluctuation caused by it easily broke through the inherent steady-state boundary, especially when pursuing a higher accuracy. However, if the steady-state boundary was artificially relaxed, although it is possible to alleviate the instability caused by control singularity, it also greatly increased the conservatism of the controller when there was no fault.

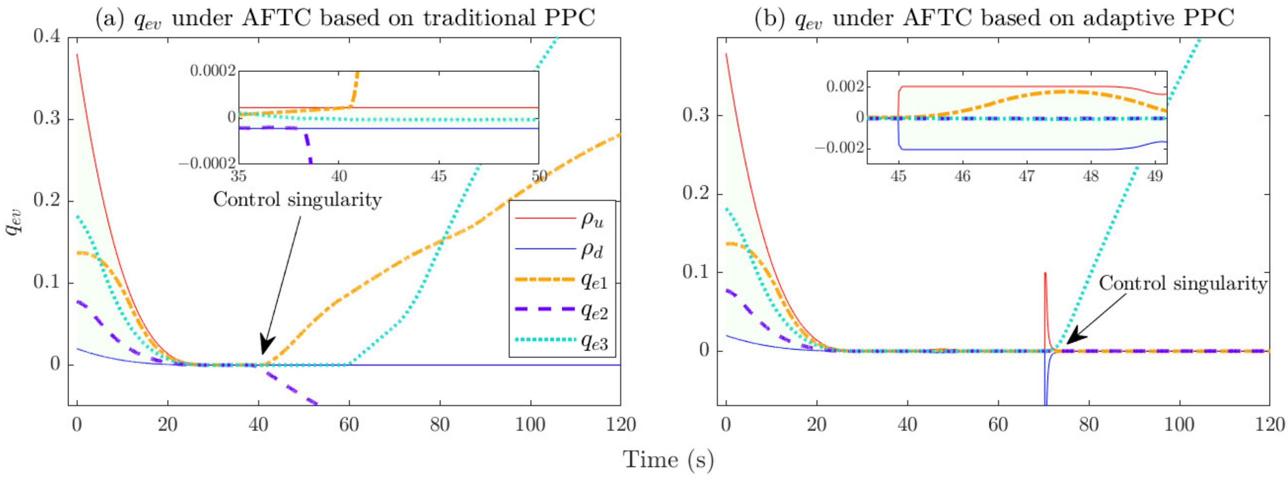

Figure 12. Time response of q_e under AFTC based on PPC and adaptive PPC in [43].

Figure 12b demonstrates the adaptive PPC in [43], the main idea of which is to judge when to relax the boundary based on the error change rate so that the error does not break through. This is applicable in smaller fault scenarios, such as the performance boundary correction at 45 s. This allowed the error to return to the expected steady-state performance after the fault disappeared. However, it should be pointed out that especially for systems with a large inertia, such as a spacecraft, it takes a long time for the effect of the fault torque to be reflected in the error change rate, which may cause the boundary correction to be untimely, and then cause the error to exceed the boundary, and thus, it cannot be recovered. Due to the lack of the direct use of fault information, it still has the probability of instability when dealing with faults. In order to measure the improvement of RPP and its impact on the computational burden, we used the time it took for the simulation program to complete all the operations in 120s as an indicator to compare. The comparison environment involved applying the traditional PPC and the RPP proposed in this paper to the same control environment (i.e., the controlled object, where the control instructions were the same). The RPP was 1.936 s, which was a negligible increase compared with the traditional PPC of 1.869 s, so the RPP almost did not require a trade-off between the performance and computing overhead.

Furthermore, it is more intuitive to convert the real-time quaternion changes of the ACS into the Euler angle form to describe the changes in the attitude of the spacecraft. As another equivalent presentation of Figure 11, Figure 13 includes the three-axis attitude target that changed with time and the actual Euler angle time response of the spacecraft. It can be seen that corresponding to Figure 11, the ACS could maneuver to the attitude target within a pre-defined time, and when the faults exceeded the actuator saturation constraint, it temporarily shifted the target and waited until the fault was resolved to maneuver back to the target attitude with the prescribed performance.

Figure 14 shows the time response of the control torque u_c. The designed control law generated appropriate torque at the right moment to drive the ACS to maneuver toward the target attitude based on the real-time actuator faults and error changes. When encountering faults, it could fully output to resist its impact and first ensure the stability of the system. When the fault was alleviated, high-precision control became the main goal again. The corresponding torque response was relatively smooth and was more in line with engineering practice. And through reasonable parameter design, the chattering phenomenon was avoided.

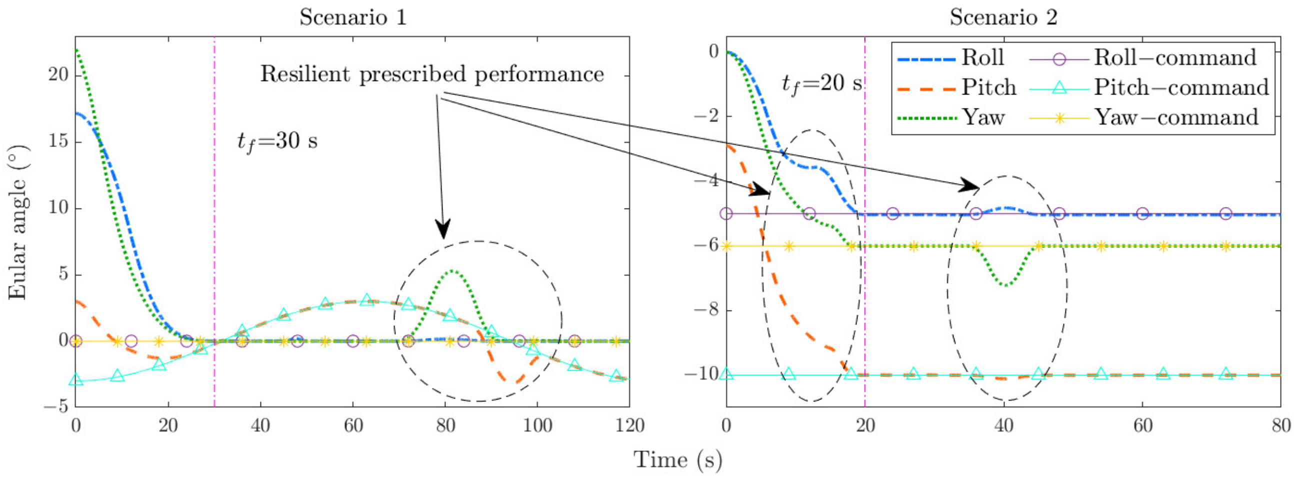

Figure 13. Euler angles time response under AFTC with RPP constraints.

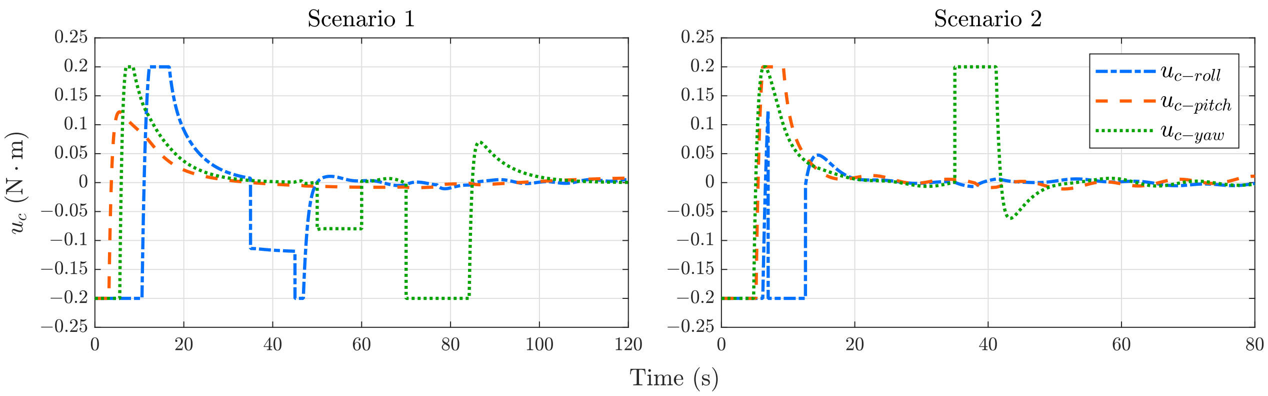

Figure 14. u_c response under AFTC with RPP constraints.

The AFTC with RPP proposed in this paper achieved a higher accuracy than the traditional method through performance constraints while achieving the performance constraints and avoiding the control singularity and inlet capture problems common in PPC. It can more conveniently realize the prescribed performance design of the controller according to needs, and has the advantages of both traditional methods and predetermined performance. Moreover, the framework proposed in this paper is highly scalable. For example, it can be further applied to the ACS with flexible components by considering liquid sloshing. The ASILO can make a unified estimate of the disturbance caused by liquid sloshing and flexible components and compensate for it by the controller. It should be noted that when there are flexible components, special care should be taken in the design of the control performance to avoid exciting low-frequency oscillations. But there are certain limitations at present, especially when $\eta_i = 1$, which means that the actuator has completely lost its output capacity. If compensation is still performed according to $\hat{f}$, the system will require the actuator to compensate for the lost torque according to the maximum output capacity. However, in a physical sense, the original framework is no longer applicable in this scenario because the actuator has no response. At this time, it is necessary to handle it through a more effective system hardware redundancy and a control allocation algorithm that fully considers the complex constraints of the actuator.

5. Conclusions

This paper proposes a novel AFTC framework, in which the proposed ASILO improved the accuracy and rapidity of fault reconstruction. It achieved good accuracy under unknown dynamic environmental interference, and the computational overhead was almost unchanged, which was more in line with the practical requirements of spacecraft. The RPP ensures fault-tolerant control with resilient performance constraints under large-scale actuator faults effectively alleviated the problems of control singularity and fault tolerance and provided higher performance and lower conservatism. It is especially suitable for scenarios with high safety requirements of spacecraft. The simulation results verified the effectiveness of the proposed framework. Future work will focus on extending the framework to more complex spacecraft with flexible components and multi-source heterogeneous actuators.

Author Contributions: Conceptualization, Z.Y. and R.J.; methodology, Z.Y. and B.Y.; software, Z.Y. and J.M.; writing—original draft preparation, Z.Y.; writing—review and editing, B.Y. and R.J.; supervision, J.M.; funding acquisition, J.M. All authors have read and agreed to the published version of the manuscript.

Funding: This work was supported in part by the National Natural Science Foundation of China under grant 61427809.

Data Availability Statement: The data are contained within the article.

Conflicts of Interest: The authors declare no conflicts of interest.

References

1. Tafazoli, M. A study of on-orbit spacecraft failures. *Acta Astronaut.* **2009**, *64*, 195–205. [CrossRef]
2. Ji, X.Y.; Li, Y.Z.; Liu, G.Q.; Wang, J.; Xiang, S.H.; Yang, X.N.; Bi, Y.Q. A brief review of ground and flight failures of Chinese spacecraft. *Prog. Aerosp. Sci.* **2019**, *107*, 19–29. [CrossRef]
3. Wang, D.; Fu, F.; Li, W.; Tu, Y.; Liu, C.; Liu, W. A review of the diagnosability of control systems with applications to spacecraft. *Annu. Rev. Control* **2020**, *49*, 212–229. [CrossRef]
4. Yin, S.; Xiao, B.; Ding, S.X.; Zhou, D. A review on recent development of spacecraft attitude fault tolerant control system. *IEEE Trans. Ind. Electron.* **2016**, *63*, 3311–3320. [CrossRef]
5. Ma, Y.; Gao, M.; Sheng, L.; Wei, Y. Active fault tolerant control for polynomial nonlinear systems with asymmetric state constraints and measurement noise. *Nonlinear Dyn.* **2023**, *111*, 14157–14175. [CrossRef]
6. Hasan, M.N.; Haris, M.; Qin, S. Fault-tolerant spacecraft attitude control: A critical assessment. *Prog. Aerosp. Sci.* **2022**, *130*, 100806. [CrossRef]
7. Abbaspour, A.; Mokhtari, S.; Sargolzaei, A.; Yen, K.K. A survey on active fault-tolerant control systems. *Electronics* **2020**, *9*, 1513. [CrossRef]
8. Fekih, A. Fault diagnosis and fault tolerant control design for aerospace systems: A bibliographical review. In Proceedings of the 2014 American Control Conference, Portland, OR, USA, 4–6 June 2014; IEEE: Piscataway, NJ, USA, 2014; pp. 1286–1291.
9. Gao, Z.; Cecati, C.; Ding, S.X. A survey of fault diagnosis and fault-tolerant techniques—Part I: Fault diagnosis with model-based and signal-based approaches. *IEEE Trans. Ind. Electron.* **2015**, *62*, 3757–3767. [CrossRef]
10. Beard, R.V. Failure Accomodation in Linear Systems Through Self-Reorganization. Ph.D. Thesis, Massachusetts Institute of Technology, Cambridge, MA, USA, 1971.
11. Patton, R.J.; Uppal, F.J.; Simani, S.; Polle, B. Robust FDI applied to thruster faults of a satellite system. *Control Eng. Pract.* **2010**, *18*, 1093–1109. [CrossRef]
12. Zhang, J.; Swain, A.K.; Nguang, S.K. Robust sensor fault estimation scheme for satellite attitude control systems. *J. Frankl. Inst.* **2013**, *350*, 2581–2604. [CrossRef]
13. Mei, Y.; Liao, Y.; Gong, K.; Luo, D. Fuzzy adaptive sliding mode fault estimation and fixed-time fault-tolerant control for coupled spacecraft based on SE (3). *Aerosp. Sci. Technol.* **2022**, *126*, 107673. [CrossRef]
14. Chen, X.; Sun, R.; Liu, M.; Song, D. Two-stage exogenous Kalman filter for time-varying fault estimation of satellite attitude control system. *J. Frankl. Inst.* **2020**, *357*, 2354–2370. [CrossRef]
15. Rahimi, A.; Kumar, K.D.; Alighanbari, H. Fault estimation of satellite reaction wheels using covariance based adaptive unscented Kalman filter. *Acta Astronaut.* **2017**, *134*, 159–169. [CrossRef]
16. Yang, Z.; Ma, J.; Ji, R.; Yang, B. Active Fault-Tolerant Control for Spacecraft with Actuator and Sensor Faults. In Proceedings of the 2022 13th Asian Control Conference (ASCC), Jeju, Republic of Korea, 4–7 May 2022; IEEE: Piscataway, NJ, USA, 2022; pp. 2410–2415.

17. Yang, Z.; Ma, J.; Ji, R.; Yang, B.; Fan, X. IAR-STSCKF-Based Fault Diagnosis and Reconstruction for Spacecraft Attitude Control Systems. *IEEE Trans. Instrum. Meas.* **2022**, *71*, 3526112. [CrossRef]
18. Chen, W.; Saif, M. Observer-based fault diagnosis of satellite systems subject to time-varying thruster faults. *J. Dyn. Sys. Meas. Control* **2007**, *129*, 352–356. [CrossRef]
19. Li, B.; Hu, Q.; Ma, G.; Yang, Y. Fault-tolerant attitude stabilization incorporating closed-loop control allocation under actuator failure. *IEEE Trans. Aerosp. Electron. Syst.* **2018**, *55*, 1989–2000. [CrossRef]
20. Zhang, Z.; Ye, D.; Xiao, B.; Sun, Z. Third-order sliding mode fault-tolerant control for satellites based on iterative learning observer. *Asian J. Control* **2019**, *21*, 43–51. [CrossRef]
21. He, T.; Wu, Z. Iterative learning disturbance observer based attitude stabilization of flexible spacecraft subject to complex disturbances and measurement noises. *IEEE/CAA J. Autom. Sin.* **2021**, *8*, 1576–1587. [CrossRef]
22. Zhu, X.; Chen, J.; Zhu, Z.H. Adaptive learning observer for spacecraft attitude control with actuator fault. *Aerosp. Sci. Technol.* **2021**, *108*, 106389. [CrossRef]
23. Ma, R.; Gui, Y.; Jia, Q.; Zheng, Z.; Li, H. Actuator Fault Identification for Spacecraft System via an Iterative Learning Observer. In *Advances in Guidance, Navigation and Control*; Springer: Singapore, 2022; pp. 4457–4466.
24. Chen, M.; Tao, G. Adaptive fault-tolerant control of uncertain nonlinear large-scale systems with unknown dead zone. *IEEE Trans. Cybern.* **2015**, *46*, 1851–1862. [CrossRef] [PubMed]
25. Wang, Y.; Liu, K.; Ji, H. Adaptive robust fault-tolerant control scheme for spacecraft proximity operations under external disturbances and input saturation. *Nonlinear Dyn.* **2022**, *108*, 207–222. [CrossRef]
26. Xiao, B.; Hu, Q.; Zhang, Y. Adaptive sliding mode fault tolerant attitude tracking control for flexible spacecraft under actuator saturation. *IEEE Trans. Control Syst. Technol.* **2011**, *20*, 1605–1612. [CrossRef]
27. Post, M.; Li, J.; Lee, R. Nanosatellite air bearing tests of fault-tolerant sliding-mode attitude control with Unscented Kalman Filter. In Proceedings of the AIAA Guidance, Navigation, and Control Conference, Minneapolis, MN, USA, 13–16 August 2012; p. 5040.
28. Van, M.; Mavrovouniotis, M.; Ge, S.S. An adaptive backstepping nonsingular fast terminal sliding mode control for robust fault tolerant control of robot manipulators. *IEEE Trans. Syst. Man, Cybern. Syst.* **2018**, *49*, 1448–1458. [CrossRef]
29. Bechlioulis, C.P.; Rovithakis, G.A. Robust partial-state feedback prescribed performance control of cascade systems with unknown nonlinearities. *IEEE Trans. Autom. Control* **2011**, *56*, 2224–2230. [CrossRef]
30. Berger, T. Input-constrained funnel control of nonlinear systems. *IEEE Trans. Autom. Control* **2024**, *69*, 5368–5382. [CrossRef]
31. Wei, C.; Chen, Q.; Liu, J.; Yin, Z.; Luo, J. An overview of prescribed performance control and its application to spacecraft attitude system. *Proc. Inst. Mech. Eng. Part I J. Syst. Control Eng.* **2021**, *235*, 435–447. [CrossRef]
32. Ji, R.; Ge, S.S. Event-Triggered Tunnel Prescribed Control for Nonlinear Systems. *IEEE Trans. Fuzzy Syst.* **2023**, *32*, 90–101. [CrossRef]
33. Zhao, K.; Chen, L.; Chen, C.P. Event-based adaptive neural control of nonlinear systems with deferred constraint. *IEEE Trans. Syst. Man, Cybern. Syst.* **2022**, *52*, 6273–6282. [CrossRef]
34. Yao, Q. Robust adaptive finite-time prescribed performance attitude tracking control of spacecraft. *Int. J. Aeronaut. Space Sci.* **2021**, *22*, 1183–1193. [CrossRef]
35. Huang, H.; He, W.; Li, J.; Xu, B.; Yang, C.; Zhang, W. Disturbance observer-based fault-tolerant control for robotic systems with guaranteed prescribed performance. *IEEE Trans. Cybern.* **2020**, *52*, 772–783. [CrossRef]
36. Ji, R.; Li, D.; Ge, S.S.; Li, H. Tunnel Prescribed Control of Nonlinear Systems with Unknown Control Directions. In *IEEE Transactions on Neural Networks and Learning Systems*; IEEE: Piscataway, NJ, USA, 2023.
37. Zhao, Q.; Duan, G. Prescribed performance tracking control for spacecraft proximity operations with inertia property identification. *Aerosp. Sci. Technol.* **2023**, *141*, 108555. [CrossRef]
38. Su, Y.; Shen, S. Adaptive global prescribed performance control for rigid spacecraft subject to angular velocity constraints and input saturation. *Nonlinear Dyn.* **2023**, *111*, 21691–21705. [CrossRef]
39. Zhang, C.L.; Guo, G. Extended prescribed performance fault-tolerant control of autonomous surface vessels using event-triggered inputs. *Nonlinear Dyn.* **2023**, *111*, 1315–1327. [CrossRef]
40. Gao, S.; Liu, X.; Jing, Y.; Dimirovski, G.M. A novel finite-time prescribed performance control scheme for spacecraft attitude tracking. *Aerosp. Sci. Technol.* **2021**, *118*, 107044. [CrossRef]
41. Shao, X.; Shi, Y.; Zhang, W. Fault-tolerant quantized control for flexible air-breathing hypersonic vehicles with appointed-time tracking performances. *IEEE Trans. Aerosp. Electron. Syst.* **2020**, *57*, 1261–1273. [CrossRef]
42. Ji, R.; Yang, B.; Ma, J.; Ge, S.S. Saturation-tolerant prescribed control for a class of mimo nonlinear systems. *IEEE Trans. Cybern.* **2021**, *52*, 13012–13026. [CrossRef]
43. Bu, X.; Hua, C.; Lv, M.; Wu, Z. Flight control of waverider vehicles with fragility-avoidance prescribed performance. *IEEE Trans. Aerosp. Electron. Syst.* **2023**, *59*, 5248–5261. [CrossRef]

44. Trakas, P.S.; Bechlioulis, C.P. Approximation-free adaptive prescribed performance control for unknown SISO nonlinear systems with input saturation. In Proceedings of the 2022 IEEE 61st Conference on Decision and Control (CDC), Cancun, Mexico, 6–9 December 2022; IEEE: Piscataway, NJ, USA, 2022; pp. 4351–4356.
45. Mei, Y.; Luo, D.; Gong, K.; Liao, Y. Disturbance observer-based event-triggered fault tolerant control for coupled spacecraft on SE (3) with actuator saturation and misalignment. *Nonlinear Dyn.* **2023**, *111*, 17987–18011. [CrossRef]
46. Liu, E.; Yan, Y.; Yang, Y. Neural network approximation-based backstepping sliding mode control for spacecraft with input saturation and dynamics uncertainty. *Acta Astronaut.* **2022**, *191*, 1–10. [CrossRef]
47. de Ruiter, A.H. Observer-based adaptive spacecraft attitude control with guaranteed performance bounds. *IEEE Trans. Autom. Control* **2015**, *61*, 3146–3151. [CrossRef]
48. Li, B.; Hu, Q.; Yu, Y.; Ma, G. Observer-based fault-tolerant attitude control for rigid spacecraft. *IEEE Trans. Aerosp. Electron. Syst.* **2017**, *53*, 2572–2582. [CrossRef]
49. Zhang, C.; Dai, M.Z.; Wu, J.; Xiao, B.; Li, B.; Wang, M. Neural-networks and event-based fault-tolerant control for spacecraft attitude stabilization. *Aerosp. Sci. Technol.* **2021**, *114*, 106746. [CrossRef]
50. Hu, J.; Huang, X.; Li, M.; Guo, M.; Xu, C.; Zhao, Y.; Liu, W.; Wang, X. Entry vehicle control system design for the Tianwen-1 mission. *Astrodynamics* **2022**, *6*, 27–37. [CrossRef]
51. Hu, Q.; Niu, G.; Wang, C. Spacecraft attitude fault-tolerant control based on iterative learning observer and control allocation. *Aerosp. Sci. Technol.* **2018**, *75*, 245–253. [CrossRef]
52. Plestan, F.; Shtessel, Y.; Bregeault, V.; Poznyak, A. New methodologies for adaptive sliding mode control. *Int. J. Control* **2010**, *83*, 1907–1919. [CrossRef]
53. Yao, Q.; Li, Q.; Huang, J.; Jahanshahi, H. PDE-based prescribed performance adaptive attitude and vibration control of flexible spacecraft. *Aerosp. Sci. Technol.* **2023**, *141*, 108504. [CrossRef]
54. An, H.; Wu, Q.; Wang, G.; Kao, Y.; Wang, C. Adaptive compound control of air-breathing hypersonic vehicles. *IEEE Trans. Aerosp. Electron. Syst.* **2020**, *56*, 4519–4532. [CrossRef]
55. Yong, K.; Chen, M.; Shi, Y.; Wu, Q. Flexible performance-based robust control for a class of nonlinear systems with input saturation. *Automatica* **2020**, *122*, 109268. [CrossRef]
56. Mitchell, I.M.; Bayen, A.M.; Tomlin, C.J. A time-dependent Hamilton-Jacobi formulation of reachable sets for continuous dynamic games. *IEEE Trans. Autom. Control* **2005**, *50*, 947–957. [CrossRef]
57. Bechlioulis, C.P.; Rovithakis, G.A. Robust adaptive control of feedback linearizable MIMO nonlinear systems with prescribed performance. *IEEE Trans. Autom. Control* **2008**, *53*, 2090–2099. [CrossRef]
58. Shen, Q.; Yue, C.; Goh, C.H.; Wang, D. Active fault-tolerant control system design for spacecraft attitude maneuvers with actuator saturation and faults. *IEEE Trans. Ind. Electron.* **2018**, *66*, 3763–3772. [CrossRef]
59. Yue, C.; Shen, Q.; Cao, X.; Wang, F.; Goh, C.H.; Lee, T.H. Fault modeling of general momentum exchange devices in spacecraft attitude control systems. *J. Frankl. Inst.* **2020**, *357*, 6407–6434. [CrossRef]